J. Fluid Mech. (2023), *vol*. 973, A24, doi:10.1017/jfm.2023.736

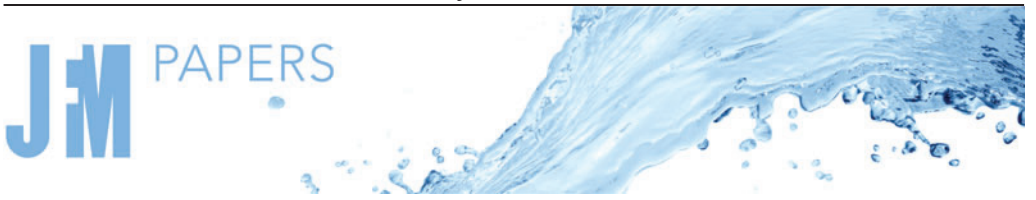

Thermocapillary dynamics of a surfactant-laden droplet with internal thermal singularity

Arindam Basak[1], **Rajaram Lakkaraju**[2] **and G.P. Raja Sekhar**[1],†

[1]Department of Mathematics, Indian Institute of Technology Kharagpur, West Bengal 721302, India

[2]TuRbulent Interfaces and Dispersion Group, Department of Mechanical Engineering, Indian Institute of Technology Kharagpur, West Bengal 721302, India

(Received 19 January 2023; revised 30 July 2023; accepted 31 August 2023)

Thermocapillary droplets with internal thermal singularities have potential applications in drug delivery and cell analysis. Inspired by the work of Pak *et al.* (*J. Fluid Mech.*, vol. 753, 2014, pp. 535–552), which was investigated for a surfactant-laden non-deformable droplet in an isothermal Poiseuille flow, we have explored the droplet dynamics by taking account of additional internal thermal singularities, namely monopole and dipole. A generalized mathematical model is developed, which is solved by using the solenoidal decomposition to describe the flow field in any arbitrary Stokes flow, and results are shown extensively for the case of a non-isothermal Poiseuille flow. Under small Péclet number (Pe_s) limit, the droplet with an off-centred monopole or a dipole oriented along the flow direction shows cross-stream migration at $O(Pe_s^2)$. However, a dipole oriented perpendicular to the flow direction results in an $O(1)$ effect due to thermocapillarity, and from $O(Pe_s)$ onwards, we observe the combined impact of thermocapillary and surfactant-induced Marangoni stresses. As a surprise, we see cross-stream migration of the droplet from the Poiseuille flow centreline in a non-isothermal field, in contrast to existing findings which rule out any cross-stream migration. We show the trade-off between thermal Marangoni number (Ma_T) and surfactant Marangoni number (Ma_Γ). Our findings on droplet dynamics inspire new possibilities for microfluidics-based design.

Key words: thermocapillarity

1. Introduction

The dynamics of suspending droplets and bubbles gained significant attention due to its vast range of applications in biomedical technology, industrial operations, bio-engineering products and microfluidic devices (Karabelas 1977; Kaushal & Tomita 2002; Stone, Stroock & Ajdari 2004; Huebner *et al.* 2008; Teh *et al.* 2008; Baroud, Gallaire

† Email address for correspondence: rajas@iitkgp.ac.in

& Dangla 2010; Seemann *et al.* 2011; Stan *et al.* 2011; Zhu & Fang 2013). In the case of cell analysis and droplet PCR, uniformly sized droplets (millimetre or sub-millimetre) are separated from the base sample, and that process depends on the flow geometry, fluid properties and external fields (such as magnetic, electric, surfactant and temperature). Droplets generally exhibit rich science in shape deformation, cross-migration, encapsulation, break-up and merging (Ahn *et al.* 2006; Link *et al.* 2006; Anna 2016; Bandopadhyay *et al.* 2016). During the droplet sorting technique, external fields are applied to create unbalanced surface forces to achieve lateral motion and separation.

The migration of droplets can also be managed without using external fields. There are droplets that migrate due to their internal activity, called 'active droplets' (Ramos, Cordero & Soto 2020; Grauer *et al.* 2021; Rajabi *et al.* 2021; Shankar, Raju & Mahadevan 2022). Studies on *Escherichia coli* encapsulated in an emulsion droplet showed motility due to internal heat generation by the micro-organism (Rothbaum & Stone 1961), which can be modelled as a droplet subjected to an internal thermal singularity. An important challenge is to find a way to control the droplet propulsion and the dependence based on the nature of singularities present (Marchetti 2012; Shankar *et al.* 2022).

Are the droplet dynamics not understood in the presence of thermal fields earlier? Partly yes, in the form of uniform or non-uniform thermal gradients in the ambient field, but without any internal thermal heating to mimic living cells cultured situation. First, we overview earlier mathematical findings on thermocapillary-based droplet dynamics, and then we proceed to explain our work on the thermal singularities. Young, Goldstein & Block (1959) have found that droplets with small Reynolds number ($Re \approx 0$) migrate from the cold to the hot side due to thermocapillary forces. Bratukhin (1975) has obtained a flow field solution up to $O(Re)$, when a constant temperature gradient is present at the far field. Thompson, DeWitt & Labus (1980) have extended the solutions up to $O(Re^2)$ and found far-field boundary conditions are difficult to satisfy similar to the Whitehead paradox. Subramanian (1983) has used the method of matched asymptotic expansions in terms of the Marangoni number (Ma) for the Stokes flow, and found the droplet velocity up to $O(Ma^2)$. Under zero gravity conditions, Balasubramaniam & Chai (1987) have shown that the solution obtained by Young *et al.* (1959) is an exact solution of the Navier–Stokes equations for any value of Re as long as Ma is small. Subramanian & Balasubramaniam (2001) indicated that the droplet migration velocity is unaffected by the surface shear viscosity but depends on the surface dilatational viscosity. Similar to thermocapillary effects, the surfactant concentration variation on the droplet interface can also alter the droplet velocity (Leal 2007). For example, a tiny surfactant presence on the droplet interface reduces the velocity (Sadhal & Johnson 1983, 1986). Hanna & Vlahovska (2010) have shown that droplets released at an arbitrary location in a Poiseuille flow (one special case of an arbitrary Stokes flow) reach the centreline for large surface Péclet numbers (Pe_s). Schwalbe *et al.* (2011) investigated the effects of surface viscosities and found that the presence of interfacial stresses significantly alters the slip velocity and the flow circulation. Dandekar & Ardekani (2020) examined the same for small Pe_s, and found that the droplet cross-stream migration is due to $O(Pe_s^2)$ terms. Das, Mandal & Chakraborty (2018) have shown that when the interfacial tension is modelled as a linear combination of surfactant and temperature, the droplet exhibits cross-stream migration at $O(Pe_s^2)$. Moreover, the direction of this motion changes depending on the thermal Marangoni number Ma_T. Sharanya, Raja Sekhar & Rohde (2019) have found that the cross-stream migration increases due to $O(Pe_s)$ if the interfacial tension is modelled as a nonlinear combination

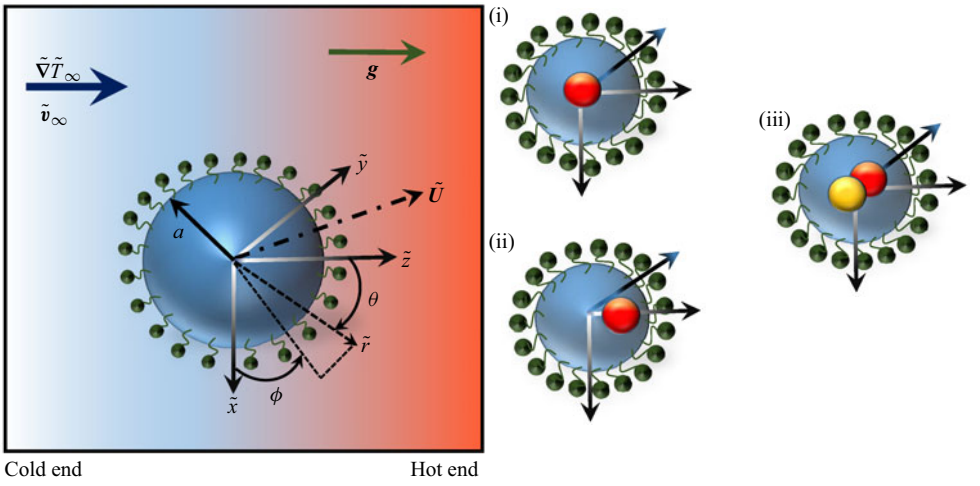

Figure 1. Schematic of a surfactant-laden droplet (of radius a) moving with velocity $\tilde{\boldsymbol{U}}$ in an ambient Stokes flow. The ambient flow has velocity $\tilde{\boldsymbol{v}}_\infty$ and is subjected to a thermal gradient $\tilde{\nabla}\tilde{T}_\infty$ (represented as a blue to red shade), coinciding with gravity $\boldsymbol{g}$. Based on the droplet centre, a spherical coordinate system $(\tilde{r}, \theta, \phi)$ is chosen that connects with a Cartesian coordinate system $(\tilde{x}, \tilde{y}, \tilde{z})$ by general transformation rule. The streamwise direction is $\tilde{z}$, and the cross-stream directions are $\tilde{x}$ (perpendicular to gravity) and $\tilde{y}$ (into the plane). In our work, droplets consist of different thermal singularities such as (i) a centred monopole, (ii) an off-centred monopole with a source in the streamwise direction, and (iii) a dipole with an arbitrary orientation. The red circle in the droplet is a hot source, and yellow for a cold sink. Surfactant is represented as a coiled ball on the droplet surface.

of surfactant and temperature field. Panigrahi *et al.* (2021) have shown that the droplet cross-stream migration gets suppressed with the inclusion of shear and dilatational surface viscosities.

To the best of our knowledge, the droplet dynamics with internal thermal singularities (due to the importance of cell separation techniques) has not been modelled yet. In this work, we have investigated a surfactant-laden droplet suspended in an arbitrary non-isothermal Stokes flow subjected to internal thermal singularities in the form of a monopole and a dipole (see figure 1). In our model, we have allowed the droplet thermophysical properties to be different from the outside ambient so that the stress and thermal balance conditions at the interface determine the droplet dynamics. We have varied the monopole location and the dipole orientation inside the droplet, and investigated the overall drag and the corresponding migration velocity. The interfacial tension in our model is a linear function of the temperature and the surfactant concentration. Our investigation highlights that in a specific arbitrary Stokes flow (i.e. a Poiseuille flow), the droplet with internal thermal singularities can show high velocity compared to the results mentioned in the previous works. Further, we have shown that the droplet can show cross-stream migration even if it is released on the Poiseuille flow centreline.

In § 2, we explain the mathematical model, corresponding boundary conditions and the parameters involved. In § 3, we outline the solution procedure using the solenoidal decomposition method for small and large Pe_s. In § 4, we investigate detailed results for droplets suspended in a non-isothermal Poiseuille flow. A summary with future scope is given in § 5.

2. Mathematical formulation

2.1. *Description of the mathematical model*

In figure 1, we have shown the schematic of a surfactant-laden droplet of radius a, suspended in an ambient flow that is subjected to an external temperature gradient $\tilde{\boldsymbol{\nabla}}\tilde{T}_\infty$. The density, dynamic viscosity, thermal conductivity and thermal diffusivity internal to the droplet are ρ^i, μ^i, κ^i and α^i, respectively. The same quantities external to the droplet are ρ^e, μ^e, κ^e and α^e, respectively. We define two coordinate systems: (1) spherical $(\tilde{r}, \theta, \phi)$ to find the detailed solutions, and (2) Cartesian $(\tilde{x}, \tilde{y}, \tilde{z})$ to show results on droplet velocity. Here, θ is the angle made by the vector $\tilde{\boldsymbol{r}}$ with the $\tilde{z}$ axis, and ϕ is the angle made by the projection of $\tilde{\boldsymbol{r}}$ on the $\tilde{x}$–$\tilde{y}$ plane with the $\tilde{x}$ axis. Consequently, we can express the relationships as $\tilde{x} = \tilde{r}\sin\theta\cos\phi$, $\tilde{y} = \tilde{r}\sin\theta\sin\phi$ and $\tilde{z} = \tilde{r}\cos\theta$. The gravitational force $\boldsymbol{g}$ acts along the $\tilde{z}$ direction. The unit vectors along the $\tilde{x}$, $\tilde{y}$ and $\tilde{z}$ directions are $\hat{i}$, $\hat{j}$ and $\hat{k}$, respectively. On a co-moving frame attached to the droplet centre, the mass, momentum and energy equations that describe internal and external flow fields satisfy (Leal 2007; Subramanian & Balasubramaniam 2001),

$$\tilde{\boldsymbol{\nabla}} \cdot \tilde{\boldsymbol{u}}^j = 0, \tag{2.1a}$$

$$\rho^j \left(\frac{\partial \tilde{\boldsymbol{u}}^j}{\partial \tilde{t}} + \tilde{\boldsymbol{u}}^j \cdot \tilde{\boldsymbol{\nabla}} \tilde{\boldsymbol{u}}^j \right) = \tilde{\boldsymbol{\nabla}} \cdot \tilde{\boldsymbol{\tau}}^j, \tag{2.1b}$$

$$\frac{\partial \tilde{T}^j}{\partial \tilde{t}} + \tilde{\boldsymbol{u}}^j \cdot \tilde{\boldsymbol{\nabla}} \tilde{T}^j = \alpha^j \tilde{\nabla}^2 \tilde{T}^j, \tag{2.1c}$$

where $j = i$ (for internal) and e (for external). The other variables are as follows: $\tilde{\boldsymbol{u}}^j$ is the relative velocity of flow with respect to the droplet centre velocity $\tilde{\boldsymbol{U}}$ (i.e. $\tilde{\boldsymbol{u}}^j = \tilde{\boldsymbol{v}}^j - \tilde{\boldsymbol{U}}$, where $\tilde{\boldsymbol{v}}^j$ is the flow velocity in the laboratory reference frame), $\tilde{\boldsymbol{\tau}}^j$ is the stress tensor, $\tilde{T}^j$ is the temperature, and $\partial/\partial\tilde{t}$ is the partial derivative with respect to time. For Newtonian fluids (as we use), the stress tensor is modelled as $\tilde{\boldsymbol{\tau}}^j = -\tilde{p}^j \boldsymbol{I} + \mu^j[\tilde{\boldsymbol{\nabla}}\tilde{\boldsymbol{u}}^j + (\tilde{\boldsymbol{\nabla}}\tilde{\boldsymbol{u}}^j)']$, where $\tilde{p}^j$ is the pressure, $\boldsymbol{I}$ is the identity tensor, $\tilde{\boldsymbol{\nabla}}$ is the gradient operator, and $'$ denotes the transpose. The surfactant concentration $\tilde{\Gamma}$ at the droplet interface $\tilde{r} = a$ satisfies (Stone & Leal 1990; Stone 1990)

$$\frac{\partial \tilde{\Gamma}}{\partial \tilde{t}} + \tilde{\boldsymbol{\nabla}}_s \cdot (\tilde{\boldsymbol{u}}_s \tilde{\Gamma}) = D_s \tilde{\boldsymbol{\nabla}}_s^2 \tilde{\Gamma}, \tag{2.2}$$

where $\tilde{\boldsymbol{u}}_s$ is the relative velocity at the surface, and D_s is the surfactant diffusivity. The surface gradient operator is $\tilde{\boldsymbol{\nabla}}_s \equiv \tilde{\boldsymbol{\nabla}} - \tilde{\boldsymbol{n}}(\tilde{\boldsymbol{n}} \cdot \tilde{\boldsymbol{\nabla}})$, for a surface described by a normal vector $\tilde{\boldsymbol{n}}$, and a tangent vector $\tilde{\boldsymbol{t}}$. The interface conditions correspond to: (1) vanishing normal velocity, $\tilde{\boldsymbol{u}}^e \cdot \tilde{\boldsymbol{n}} = \tilde{\boldsymbol{u}}^i \cdot \tilde{\boldsymbol{n}} = 0$; (2) continuity in tangential velocity, $\tilde{\boldsymbol{u}}^e \cdot \tilde{\boldsymbol{t}} - \tilde{\boldsymbol{u}}^i \cdot \tilde{\boldsymbol{t}} = 0$; and (3) jump in the tangential stress, $\tilde{\boldsymbol{\tau}}^e \cdot \tilde{\boldsymbol{n}} \cdot \tilde{\boldsymbol{t}} - \tilde{\boldsymbol{\tau}}^i \cdot \tilde{\boldsymbol{n}} \cdot \tilde{\boldsymbol{t}} = -\tilde{\boldsymbol{\nabla}}_s \tilde{\sigma} \cdot \tilde{\boldsymbol{t}}$. The interfacial tension $(\tilde{\sigma})$ in our work is modelled as $\tilde{\sigma}(\tilde{T}) = \tilde{\sigma}_0 - \gamma(\tilde{T} - \tilde{T}_0) - R_g \tilde{T}_0 \tilde{\Gamma}$ for the dilute concentrations and moderate temperature differences (Homsy & Meiburg 1984; Kim & Subramanian 1989; Leal 2007). The equilibrium interfacial tension $(\tilde{\sigma}_0)$ is considered at reference temperature $\tilde{T}_0$, γ is a positive constant, and R_g is the ideal gas constant. The temperature field at the interface satisfies $\tilde{T}^e = \tilde{T}^i$ and $\kappa^e(\partial\tilde{T}^e/\partial\tilde{r}) = \kappa^i(\partial\tilde{T}^i/\partial\tilde{r})$. The far-field conditions (at $\tilde{r} \to \infty$) for the velocity, pressure and temperature are $\tilde{\boldsymbol{u}}^e \to \tilde{\boldsymbol{u}}_\infty = \tilde{\boldsymbol{v}}_\infty - \tilde{\boldsymbol{U}}$, $\tilde{p}^e \to \tilde{p}_\infty$ and $\tilde{T}^e \to \tilde{T}_\infty$, respectively. Internal to the droplet (at

$\tilde{r} \to 0$), both the velocity $\tilde{\boldsymbol{u}}^i$ and the pressure $\tilde{p}^i$ are bounded, and the temperature satisfies, $\tilde{T}^i \to \tilde{T}_s$, for a prescribed thermal source that generates temperature $\tilde{T}_s$.

2.2. *Control parameters and dimensionless governing equations*

To non-dimensionalize the variables, we need to define relevant characteristic quantities. For example, in a cylindrical Poiseuille flow of radius $\tilde{R}_0$ with the centreline flow velocity U_c, we define the dimensionless variables as $\boldsymbol{u}^j = \tilde{\boldsymbol{u}}^j/U_c$, $\boldsymbol{\nabla} = a\,\tilde{\boldsymbol{\nabla}}$, $\boldsymbol{r} = \tilde{\boldsymbol{r}}/a$, $p^j = \tilde{p}^j/(\mu^e U_c/a)$, $\sigma = \tilde{\sigma}/\tilde{\sigma}_0$, $T^j = (\tilde{T}^j - \tilde{T}_0)/a\,|\tilde{\boldsymbol{\nabla}}\tilde{T}^\infty|$, $\Gamma = \tilde{\Gamma}/\tilde{\Gamma}_0$ and $t = \tilde{t}/(\tilde{R}_0/U_c)$. Here, $\tilde{R}_0/U_c$ denotes the advection time scale. With these non-dimensional variables, the governing equations (2.1) reduce to

$$\boldsymbol{\nabla}\cdot\boldsymbol{u}^j = 0, \tag{2.3a}$$

$$Re\,(\rho^j/\rho^e)\left[\frac{a}{\tilde{R}_0}\frac{\partial \boldsymbol{u}^j}{\partial t} + (\boldsymbol{u}^j\cdot\boldsymbol{\nabla}\boldsymbol{u}^j)\right] = -\boldsymbol{\nabla}p^j + (\mu^j/\mu^e)\,\nabla^2\boldsymbol{u}^j, \tag{2.3b}$$

$$Pe_T\left[\frac{a}{\tilde{R}_0}\frac{\partial T^j}{\partial t} + (\boldsymbol{u}^j\cdot\boldsymbol{\nabla}T^j)\right] = (\alpha^j/\alpha^e)\,\nabla^2 T^j, \tag{2.3c}$$

where Re ($\equiv \rho^e U_c a/\mu^e$) is the Reynolds number, and Pe_T ($\equiv U_c a/\alpha^e$) is the thermal Péclet number. Note that index $j = i$ for the internal flow and e for the external flow.

The surfactant transport equation (2.2) in dimensionless form is

$$Pe_s\left[\frac{a}{\tilde{R}_0}\frac{\partial \Gamma}{\partial t} + \boldsymbol{\nabla}_s\cdot(\Gamma\boldsymbol{u}_s)\right] = \nabla_s^2\Gamma, \tag{2.4}$$

where Pe_s ($\equiv U_c a/D_s$) is the surface Péclet number. The interface conditions (at $r = 1$) in dimensionless form are: (1) $\boldsymbol{u}^e\cdot\tilde{\boldsymbol{n}} = \boldsymbol{u}^i\cdot\tilde{\boldsymbol{n}} = 0$, (2) $\boldsymbol{u}^e\cdot\tilde{\boldsymbol{t}} - \boldsymbol{u}^i\cdot\tilde{\boldsymbol{t}} = 0$, and (3) $\boldsymbol{\tau}^e\cdot\tilde{\boldsymbol{n}}\cdot\tilde{\boldsymbol{t}} - \mu\,\boldsymbol{\tau}^i\cdot\tilde{\boldsymbol{n}}\cdot\tilde{\boldsymbol{t}} = \boldsymbol{\nabla}_s(Ma_T\,T^e + Ma_\Gamma\,\Gamma)\cdot\tilde{\boldsymbol{t}}$, where $\mu = \mu^i/\mu^e$, $Ma_T = \gamma\,|\tilde{\boldsymbol{\nabla}}\tilde{T}_\infty|\,a/\mu^e U_c$ is the thermal Marangoni number, and $Ma_\Gamma = R_g\tilde{T}_0\tilde{\Gamma}_0/\mu^e U_c$ is the surfactant Marangoni number. Note that the tangential stress balance condition is simplified using $\sigma = 1 - Ca\,(Ma_T\,T + Ma_\Gamma\,\Gamma)$, where $Ca = \mu^e U_c/\tilde{\sigma}_0$ is the capillary number. The thermal field at the interface satisfies $T^e = T^i$ and $\partial T^e/\partial r = \kappa\,(\partial T^i/\partial r)$, where $\kappa = \kappa^i/\kappa^e$. The far-field conditions (at $r \to \infty$) are $\boldsymbol{u}^e \to \boldsymbol{u}_\infty = \boldsymbol{v}_\infty - \boldsymbol{U}$, $p^e \to p_\infty$, and $T^e \to T_\infty$. Internal to the droplet (as $r \to 0$), we have $\boldsymbol{u}^i$ and p^i bounded with $T^i \to T_s$, the thermal singularity.

To give an idea about the mentioned dimensionless numbers, we discuss two examples: (1) a thermocapillary droplet (Nallani & Subramanian 1993) of radius 50–146 µm suspended in an ambient fluid with $\rho^e = 955\,\mathrm{kg\,m^{-3}}$, $\mu^e = 0.0478\,\mathrm{N\,s\,m^{-2}}$, $\kappa^e = 0.1\,\mathrm{W\,m^{-1}\,K^{-1}}$; and (2) a deionized water droplet (Panigrahi *et al.* 2021) suspended in another medium with the properties $\rho^e = 971\,\mathrm{kg\,m^{-3}}$, $\mu^e = 0.04855\,\mathrm{N\,s\,m^{-2}}$, $\alpha^e = 7\times10^{-8}\,\mathrm{m^2\,s^{-1}}$, $D_s = 10^{-11}$–$10^{-8}\,\mathrm{m^2\,s^{-1}}$ and $\tilde{\Gamma}_0 = 10^{-10}$–$10^{-6}\,\mathrm{mol\,m^{-2}}$. Based on these examples, the corresponding parameter ranges are ρ ($= \rho^i/\rho^e$) $\sim O(10^{-2})$–$O(1)$, $Re \sim O(10^{-4})$, $a/\tilde{R}_0 \sim O(10^{-2})$, $\mu \sim O(10^{-2})$–$O(10^2)$, $Pe_T \sim O(10^{-2})$, α ($= \alpha^i/\alpha^e$) $\sim O(10^{-1})$–$O(1)$, $Pe_s \sim O(10^{-1})$–$O(10^2)$, $Ma_T \sim O(10^{-2})$ –$O(10^1)$, $Ma_\Gamma \sim O(10^{-2})$–$O(10^2)$ and $Ca \sim O(10^{-4})$. Further, this study focuses on droplet dynamics in situations where droplets may have a density different from the

surrounding medium. The presence of gravity leads to a buoyancy effect, causing droplets to undergo motion. When gravity acts perpendicular to the flow, the cross-stream velocity of a buoyant droplet is governed primarily by the buoyancy force, and the effects of flow and temperature field are negligible. Consequently, investigating buoyant droplets in such systems is considered less important. However, here we explore specifically droplet migration when gravity acts in the same direction as the imposed flow (as depicted in figure 1). This scenario presents an intriguing area of research to understand the dynamics and behaviour of buoyant droplets under these conditions. Thus we have the Bond number $Bo = |\rho^i - \rho^e|\, g a^2/\tilde{\sigma}_0$, which is of $O(10^{-4})$. Note that the normal stress balance determines the droplet shape (Hetsroni & Haber 1970), and due to small $Ca \sim O(10^{-4})$, we have assumed that the droplet is spherical.

Considering $Re \sim O(10^{-4})$, we have neglected terms with $(a/\tilde{R}_0)\, Re$ since they are significantly smaller than Re itself. Similarly, in the energy equation, considering the value of $Pe_T \sim O(10^{-2})$, we have disregarded terms with $(a/\tilde{R}_0)\, Pe_T$ as they are much smaller compared to Pe_T. Thus the governing equations become

$$\boldsymbol{\nabla} \cdot \boldsymbol{u}^j = 0, \tag{2.5a}$$

$$-\boldsymbol{\nabla} p^j + (\mu^j/\mu^e)\, \nabla^2 \boldsymbol{u}^j = 0, \tag{2.5b}$$

$$\nabla^2 T^j = 0. \tag{2.5c}$$

With reference to the surfactant transport equation given in (2.2), the order of magnitude analysis of the individual terms indicates that when the advection time scale is restricted as $\tilde{R}_0/U_c \gg l_c/U_c$, the governing equation reaches a quasi-steady state. Accordingly, for the choice $l_c = a \ll \tilde{R}_0$ (small droplets), we ensure that $a/U_c \ll \tilde{R}_0/U_c$. Consequently, we can neglect the transient terms, resulting in the simplified surfactant transport equation

$$Pe_s\, \boldsymbol{\nabla}_s \cdot (\Gamma \boldsymbol{u}_s) = \nabla_s^2 \Gamma. \tag{2.6}$$

We have considered that the surfactant concentration satisfies the condition $\int_{\phi=0}^{2\pi} \int_{\theta=0}^{\pi} \Gamma(\theta, \phi) \sin\theta \, \mathrm{d}\theta \, \mathrm{d}\phi = 4\pi$. We can solve (2.6) analytically for a few special cases like small and large Pe_s. The surface diffusion dominates the transport for $Pe_s \ll 1$, and the surface convection dominates the transport for $Pe_s \gg 1$.

3. Solution procedure

Irrespective of the values of Pe_s, the temperature field is independent of the flow field and the surfactant concentration; thus we first solve the temperature equations with the prescribed boundary and interface conditions. Using asymptotic perturbation for small and large Pe_s, we solve the surfactant concentration and flow fields simultaneously (see figure 2). At each order of perturbation, the Stokes flow equations are solved using the solenoidal decomposition method known as the double-curl method, which is described briefly in § 3.2. In the subsequent subsections, we provide the necessary details about the solution procedure to determine the drag on the surface of the droplet and the corresponding migration velocity.

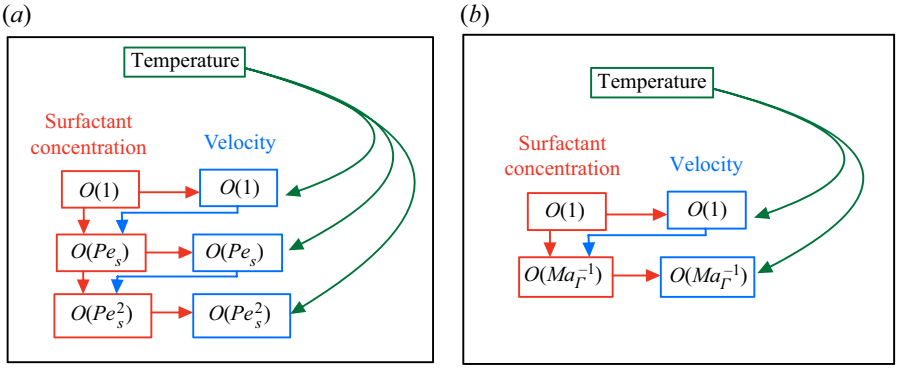

Figure 2. Schematic of a general procedure to solve for velocity $\boldsymbol{u}$ and surfactant concentration Γ from the temperature field T, for (*a*) small-Pe_s limit, and (*b*) large-Pe_s limit. Step-by-step progression in arrows, where each quantity is solved before moving on to the next one. Temperature and previous quantities are utilized at each step, and Ma_Γ is the surfactant-based Marangoni number.

3.1. *Thermal field*

Both inside and outside of the droplet satisfy the Laplace equation (2.5*c*) with a complete general solution in the form

$$T^i = \sum_{n=0}^{\infty} \left(a_n r^n + \frac{b_n}{r^{n+1}} \right) \mathcal{S}_n(\theta, \phi) \quad \text{and} \quad T^e = \sum_{n=0}^{\infty} \left(c_n r^n + \frac{d_n}{r^{n+1}} \right) \mathcal{S}_n(\theta, \phi), \tag{3.1a,b}$$

where $\mathcal{S}_n(\theta, \phi) = \sum_{m=0}^{n} P_n^m(\cos\theta)(A_{nm}\cos m\phi + B_{nm}\sin m\phi)$ is the nth spherical harmonic, $P_n^m(\cos\theta)$ is the associated Legendre polynomial, and A_{nm}, B_{nm} are the known scalars (Sneddon 2006). In (3.1*a*,*b*), a_n and d_n are to be determined using the thermal interface conditions at $r = 1$, whereas b_n comes from the internal thermal singularity and c_n from the ambient far field, respectively. We consider the chosen thermal singularity and the far-field condition to satisfy the Laplace equation such that

$$T_s = \sum_{n=0}^{\infty} \frac{b_n}{r^{n+1}} \mathcal{S}_n(\theta, \phi) \text{ at } r = 0, \quad \text{and} \quad T_\infty = \sum_{n=0}^{\infty} c_n r^n \mathcal{S}_n(\theta, \phi) \text{ at } r \to \infty. \tag{3.2a,b}$$

Further, T_s varies depending on the type of singularity chosen. For example, a monopole of strength S located at the droplet centre ($r = 0$) corresponds to $T_s = S/r$, which is the free-space Green's function in $\mathbb{R}^3$ of the Laplace equation. If the monopole is off-centred by a distance d along the flow direction with $0 < d < 1$, then we have $T_s = \sum_{n=0}^{\infty} S(d^n/r^{n+1})\, P_n(\cos\theta)$. A dipole (which is a combination of a sink and a source of equal strength S) located at the droplet centre and oriented at an arbitrary angle in spherical coordinates creates a thermal field,

$$T_s = \frac{1}{r^2}[P_1^0(\cos\theta)\,(S\cos\theta) + P_1^1(\cos\theta)\,(S\sin\theta\cos\phi + S\sin\theta\sin\phi)]. \tag{3.3}$$

We have estimated the required non-zero coefficients as follows: for a centred monopole, $b_0 A_{00} = S$; for an off-centred monopole, $b_n A_{n0} = Sd^n$ for all $n \geq 0$; and for a dipole, we have $b_1 A_{11} = S\sin\theta\cos\phi$, $b_1 B_{11} = S\sin\theta\sin\phi$ and $b_1 A_{10} = S\cos\theta$ for fixed θ and ϕ. All other coefficients not explicitly mentioned here are zero.

The far-field temperature gradient is essential in determining the particular flow behaviour and heat transfer. A constant temperature gradient simplifies the thermal boundary conditions at infinity. Further, it gives a more accurate solution by ensuring that the flow field is symmetric and uniform. Following Choudhuri & Raja Sekhar (2013) and Sharanya & Raja Sekhar (2015), we can write the temperature field corresponding to the constant far-field temperature gradient as $T_\infty = Gr\cos\theta$, where $G < 0$ for a decrease in temperature along the flow direction, and $G > 0$ otherwise. Consequently, we find that $c_1 A_{10} = G$ and the remaining c_n are zero, for all $n \neq 1$. By applying the interface conditions, we get the coefficients

$$a_n = \frac{(2n+1)c_n + (n+1)(\kappa-1)b_n}{(n\kappa+n+1)} \quad \text{and} \quad d_n = \frac{n(1-\kappa)c_n + \kappa(2n+1)b_n}{(n\kappa+n+1)}. \tag{3.4a,b}$$

This determines the thermal field interior and exterior of the droplet due to thermal singularities.

3.2. *Double-curl strategy to obtain the velocity field*

It is important to note that Lamb's general solution (Lamb 1924) helps to solve any arbitrary steady Stokes flow, in which velocity and pressure fields are represented as a series of an infinite number of harmonic scalar functions. As an alternative, Palaniappan *et al.* (1992), Raja Sekhar *et al.* (1995) and Padmavathi, Raja Sekhar & Amaranath (1998) developed the double-curl method, which is a complete general solution framework to solve the Stokes equations, in which the velocity and the pressure fields are represented in terms of a scalar biharmonic function and a scalar harmonic function. Correspondingly, the velocity and the pressure fields of the Stokes equation are represented as $\boldsymbol{u} = \boldsymbol{\nabla}\times\boldsymbol{\nabla}\times(\boldsymbol{r}A) + \boldsymbol{\nabla}\times(\boldsymbol{r}B)$ and $p = p_\infty + (\partial/\partial r)(r\nabla^2 A)$. The scalars A and B satisfy $\nabla^4 A = 0$ and $\nabla^2 B = 0$. The general solutions for A and B are expressed in terms of the basis vectors, $\{r^n, r^{n+2}, r^{-(n+1)}, r^{-(n-1)}\}\,\mathcal{R}_n(\theta,\phi)$ and $\{r^n, r^{-(n+1)}\}\,\mathcal{T}_n(\theta,\phi)$ for all $n \geq 0$, respectively. Here, $\mathcal{R}_n(\theta,\phi) = \sum_{m=0}^{n} P_n^m(\cos\theta)\,(C_{nm}\cos m\phi + D_{nm}\sin m\phi)$ and $\mathcal{T}_n(\theta,\phi) = \sum_{m=0}^{n} P_n^m(\cos\theta)\,(E_{nm}\cos m\phi + F_{nm}\sin m\phi)$ are the spherical harmonics, where C_{nm}, D_{nm}, E_{nm} and F_{nm} are constants (which are determined from the spherical harmonics at the far field). Using the superscripts e and i to denote external and internal quantities, respectively, the interface conditions (at $r = 1$) in terms of the scalars are given by $A^e = 0$, $A^i = 0$, $\partial A^e/\partial r = \partial A^i/\partial r$, $B^e = B^i$, $\partial^2 A^e/\partial r^2 - \mu(\partial^2 A^i/\partial r^2) = Ma_T T^e + Ma_\Gamma \Gamma$ and $(\partial/\partial r)(B^e/r) = \mu(\partial/\partial r)(B^i/r)$. We have $A^i < \infty$, $B^i < \infty$ for $r \to 0$, and from the far-field conditions, we infer $A^e \to A_\infty$ and $B^e \to B_\infty$. In series form, we have

$$A_\infty = \sum_{n=0}^{\infty}(\alpha_n^\infty r^n + \hat{\alpha}_n^\infty r^{n+2})\,\mathcal{R}_n(\theta,\phi) \quad \text{and} \quad B_\infty = \sum_{n=0}^{\infty}\chi_n^\infty r^n\,\mathcal{T}_n(\theta,\phi), \tag{3.5a,b}$$

where α_n^∞, $\hat{\alpha}_n^\infty$ and χ_n^∞ are known coefficients determined by the choice of a particular Stokes flow at the far field. The resultant flow interior ($r < 1$) and exterior ($r > 1$) of the

drop follow:

$$A^i = \sum_{n=0}^{\infty} (\delta_n r^n + \hat{\delta}_n r^{n+2})\, \mathcal{R}_n(\theta, \phi) \quad \text{and} \quad B^i = \sum_{n=0}^{\infty} \gamma_n r^n\, \mathcal{T}_n(\theta, \phi), \tag{3.6a,b}$$

$$A^e = A_\infty + \sum_{n=0}^{\infty} \left(\frac{\beta_n}{r^{n+1}} + \frac{\hat{\beta}_n}{r^{n-1}} \right) \mathcal{R}_n(\theta, \phi) \quad \text{and} \quad B^e = B_\infty + \sum_{n=0}^{\infty} \frac{\zeta_n}{r^{n+1}}\, \mathcal{T}_n(\theta, \phi), \tag{3.7a,b}$$

where δ_n, $\hat{\delta}_n$, γ_n, β_n, $\hat{\beta}_n$ and ζ_n are the unknown coefficients that are to be determined using the interface conditions. Consequently, we can compute the velocity and pressure fields. The next task is to compute the migration velocity of the droplet. Towards this, we use the force-free condition (Happel & Brenner 1981) on the droplet, which corresponds to the balance between the drag ($\boldsymbol{D}^H$) and the buoyancy force as

$$\underbrace{\int_\Omega \boldsymbol{\tau}^e \cdot \tilde{\boldsymbol{n}}\, \mathrm{d}\Omega}_{\textit{Hydrodynamic drag}} + \underbrace{\frac{4\pi}{3} \frac{Bo}{Ca}\, \boldsymbol{\omega}}_{\textit{Buoyancy}} = 0, \tag{3.8}$$

where $\mathrm{d}\Omega$ is the droplet surface element, $\boldsymbol{\omega}$ denotes the direction of the buoyancy force, and the denser fluid among the droplet and the surrounding phase is determined by the magnitude ω. If $\omega = 1$, then the drop is denser than the suspending phase ($\rho^i > \rho^e$), and if $\omega = -1$, then the surrounding fluid is dense ($\rho^i < \rho^e$).

3.3. *A regular perturbation of the surfactant transport and droplet velocity*

To compute drag and droplet velocity, we need surfactant distribution and flow field. The surfactant transport equation (2.6) and the scalars A^j and B^j are coupled via the interface conditions. A complete analytical solution for the entire range of Pe_s is not possible, hence we construct an asymptotic solution for $Pe_s \ll 1$ and $Pe_s \gg 1$ as a regular perturbation problem.

3.3.1. *For small surface Péclet number ($Pe_s \ll 1$)*

In the limit $Pe_s \ll 1$, the surfactant concentration and velocity can be expanded in terms of a regular perturbation in Pe_s as (Pak, Feng & Stone 2014; Sharanya *et al.* 2019)

$$\left[\Gamma, \boldsymbol{u}^j\right] = \underbrace{\left[\Gamma_0, \boldsymbol{u}_0^j\right]}_{\textit{Leading order}} + Pe_s \underbrace{\left[\Gamma_1, \boldsymbol{u}_1^j\right]}_{\textit{First order}} + Pe_s^2 \underbrace{\left[\Gamma_2, \boldsymbol{u}_2^j\right]}_{\textit{Second order}} + O(Pe_s^3). \tag{3.9}$$

From (2.6) and (3.9), the surfactant transport equation at various orders follows:

$$O(1): \quad \nabla_s^2 \Gamma_0 = 0, \tag{3.10a}$$

$$O(Pe_s): \quad \nabla_s^2 \Gamma_1 = \nabla_s \cdot (\boldsymbol{u}_{s,0} \Gamma_0), \tag{3.10b}$$

$$O(Pe_s^2): \quad \nabla_s^2 \Gamma_2 = \nabla_s \cdot (\boldsymbol{u}_{s,0} \Gamma_1 + \boldsymbol{u}_{s,1} \Gamma_0), \tag{3.10c}$$

where $\boldsymbol{u}_{s,0}$ and $\boldsymbol{u}_{s,1}$ are the surface velocities at the leading order and first order in Pe_s, respectively. From the first order onwards, the surfactant concentration depends

on the previous flow field (or the surface velocity) and the surfactant concentration of the previous order, and appears as a non-homogeneous part to the Laplacian as in (3.10*b*) and (3.10*c*). The leading-order surfactant transport equation (3.10*a*), which further satisfies the mass balance condition, follows $\Gamma_0 = 1$. The leading-order velocity and pressure fields are computed using the double-curl strategy by applying the interface and far-field conditions. The first-order surfactant transport equation is solved by using already computed leading-order results. Further details in terms of spherical harmonics are shown in Appendix A.

The leading-order drag $\boldsymbol{D}_0^H$ obtained by using (3.8), in the form of Faxen's laws (Subramanian & Balasubramaniam 2001) is

$$\boldsymbol{D}_0^H = 6\pi \left(\frac{3\mu + 2}{3(\mu + 1)} [\boldsymbol{u}_{\infty,0}]_0 + \frac{\mu}{6(\mu + 1)} [\nabla^2 \boldsymbol{u}_{\infty,0}]_0 + \frac{2Ma_T}{3(\mu + 1)(\kappa + 2)} [\boldsymbol{\nabla} T_\infty]_0 + \frac{2\kappa \mathscr{b}_1 Ma_T}{3(\mu + 1)(\kappa + 2)} \boldsymbol{Y}_0 \right), \tag{3.11}$$

with zero net torque. The detailed expressions of $[\boldsymbol{u}_{\infty,0}]_0$, $[\nabla^2 \boldsymbol{u}_{\infty,0}]_0$, $[\boldsymbol{\nabla} T_\infty]_0$ and $\boldsymbol{Y}_0$ are given in (A2) and (A3). Note that the fourth term in the above equation signifies the role of internal thermal singularity.

The leading-order migration velocity of the drop is found by equating the drag force to zero, which gives

$$\boldsymbol{U}_0 = \underbrace{[\boldsymbol{v}_{\infty,0}]_0 + \left(\frac{\mu}{6\mu + 4} \right) [\nabla^2 \boldsymbol{v}_{\infty,0}]_0}_{\textit{Ambient flow contribution}} + \underbrace{\frac{2Ma_T}{(3\mu + 2)(\kappa + 2)} [\boldsymbol{\nabla} T_\infty]_0}_{\textit{Thermal gradient contribution}} + \underbrace{\frac{2\kappa \mathscr{b}_1 Ma_T}{(3\mu + 2)(\kappa + 2)} \boldsymbol{Y}_0}_{\substack{\textit{Internal thermal} \\ \textit{singularity contribution}}} + \underbrace{\boldsymbol{U}_{B,0}}_{\substack{\textit{Buoyancy} \\ \textit{contribution}}}. \tag{3.12}$$

Here, $\boldsymbol{U}_{B,0}$ is the velocity contribution due to the buoyancy, which depends on the particular ambient flow (a detailed analysis for Poiseuille flow is provided in Appendix B). The structure in (3.12) allows us to compute the droplet velocity for any arbitrary ambient flow and thermal fields in the presence of thermal singularities interior to the droplet. Hence the expression (3.12) for the migration velocity facilitates a more generalized control of the drop migration based on the choice of various parameters involved. At the leading order, we have $\Gamma_0 = 1$, and $\boldsymbol{\nabla}_s \Gamma_0 = \boldsymbol{0}$, so the surfactant coating is uniform on the drop surface. Hence there is no influence of surfactant-induced Marangoni stresses on the droplet migration velocity.

Following the same approach, we find the first-order drag $\boldsymbol{D}_1^H$ and droplet migration velocity $\boldsymbol{U}_1$ as

$$\boldsymbol{D}_1^H = 2\pi \left[-\left(\frac{2 + 3\mu}{\mu + 1} \right) \boldsymbol{U}_1 + \frac{2}{3(\mu + 1)} Ma_\Gamma \boldsymbol{Y}_1 \right], \tag{3.13a}$$

$$\boldsymbol{U}_1 = \frac{2}{3(3\mu + 2)} Ma_\Gamma \boldsymbol{Y}_1 + \boldsymbol{U}_{B,1}, \tag{3.13b}$$

where the complete expression of the vector $\boldsymbol{Y}_1$ is given in (A7).

The second-order drag $\boldsymbol{D}_2^H$ and the migration velocity $\boldsymbol{U}_2$ are

$$\boldsymbol{D}_2^H = 2\pi\left[-\left(\frac{2+3\mu}{\mu+1}\right)\boldsymbol{U}_2 + \frac{2}{3(\mu+1)}\,Ma_\Gamma\,\boldsymbol{Y}_2\right], \tag{3.14a}$$

$$\boldsymbol{U}_2 = \frac{2}{3(3\mu+2)}\,Ma_\Gamma\,\boldsymbol{Y}_2 + \boldsymbol{U}_{B,2}, \tag{3.14b}$$

where the vector $\boldsymbol{Y}_2$ is given in (A10). Further, $\boldsymbol{U}_{B,1}$ and $\boldsymbol{U}_{B,2}$ are due to buoyancy and depend on the background flow. The impact of the non-uniform surfactant distribution is reflected in the migration velocity of the droplet at first and second order. A closer look at the structures of $\boldsymbol{Y}_1$ and $\boldsymbol{Y}_2$ (refer to Appendix A) reveals that the presence of thermal singularities affects the migration velocity. The results given in (3.11), (3.12), (3.13*a*), (3.13*b*), (3.14*a*) and (3.14*b*) are more generic and can be used for any arbitrary Stokes flow.

3.3.2. *For large surface Péclet number ($Pe_s \gg 1$)*

For large Pe_s ($\gg 1$), the surfactant transport equation (2.6) simplifies to

$$\boldsymbol{\nabla}_s \cdot (\boldsymbol{u}_s \Gamma) = 0, \tag{3.15}$$

with a thin mass transfer boundary layer structure very close to the drop. For large surfactant Marangoni number ($Ma_\Gamma \gg 1$), we can expand the surfactant concentration and velocity fields as a regular perturbation with the form (Hanna & Vlahovska 2010; Schwalbe *et al.* 2011)

$$[\Gamma, \boldsymbol{u}^j] = [\Gamma_0, \boldsymbol{u}_0^j] + Ma_\Gamma^{-1}\,[\Gamma_1, \boldsymbol{u}_1^j] + Ma_\Gamma^{-2}\,[\Gamma_2, \boldsymbol{u}_2^j] + O(Ma_\Gamma^{-3}). \tag{3.16}$$

The leading-order surfactant concentration follows $\Gamma_0 = 1$ (Hanna & Vlahovska 2010; Schwalbe *et al.* 2011). Substituting (3.16) in (3.15), the governing equations for surfactant concentration at different orders are

$$O(1): \quad \boldsymbol{\nabla}_s \cdot \boldsymbol{u}_{s,0} = 0, \tag{3.17a}$$

$$O(Ma_\Gamma^{-1}): \quad \boldsymbol{\nabla}_s \cdot \left(\boldsymbol{u}_{s,0}\Gamma_1 + \boldsymbol{u}_{s,1}\right) = 0. \tag{3.17b}$$

The flow field is unaffected by the above expansion except for the tangential stress condition at the interface. In leading and first order, the relevant tangential stress conditions are

$$O(1): \quad (\boldsymbol{\tau}^e \cdot \tilde{\boldsymbol{n}} \cdot \tilde{\boldsymbol{t}})_0 - \mu(\boldsymbol{\tau}^i \cdot \tilde{\boldsymbol{n}} \cdot \tilde{\boldsymbol{t}})_0 = \boldsymbol{\nabla}_s(Ma_T\, T^e + \Gamma_1) \cdot \tilde{\boldsymbol{t}}, \tag{3.18a}$$

$$O(Ma_\Gamma^{-1}): \quad (\boldsymbol{\tau}^e \cdot \tilde{\boldsymbol{n}} \cdot \tilde{\boldsymbol{t}})_1 - \mu(\boldsymbol{\tau}^i \cdot \tilde{\boldsymbol{n}} \cdot \tilde{\boldsymbol{t}})_1 = \boldsymbol{\nabla}_s\Gamma_2 \cdot \tilde{\boldsymbol{t}}. \tag{3.18b}$$

Further, the perturbation expansion does not have any impact on the thermal field. Hence the solution of the thermal field is the same as that presented in § 3.1. The flow field follows a procedure similar to that described for the small surface Péclet number case, except for the tangential stress jump condition. The detailed expressions for the surfactant distribution and the velocity field are given in § A.2.

The leading-order drag and the droplet migration velocity corresponding to (3.16) are

$$\boldsymbol{D}_0^H = 6\pi([\boldsymbol{u}_{\infty,0}]_0 + \tfrac{1}{6}[\nabla^2\boldsymbol{u}_{\infty,0}]_0) \quad \text{and} \quad \boldsymbol{U}_0 = [\boldsymbol{v}_{\infty,0}]_0 + \tfrac{1}{6}[\nabla^2\boldsymbol{v}_{\infty,0}]_0 + \boldsymbol{U}_{B,0}. \tag{3.19a,b}$$

We can observe that in the limit as $\mu \to \infty$, (3.11) and (3.12) reduce to (3.19*a*,*b*). In this context, we refer to Manikantan & Squires (2020), where the large Ma_Γ limit

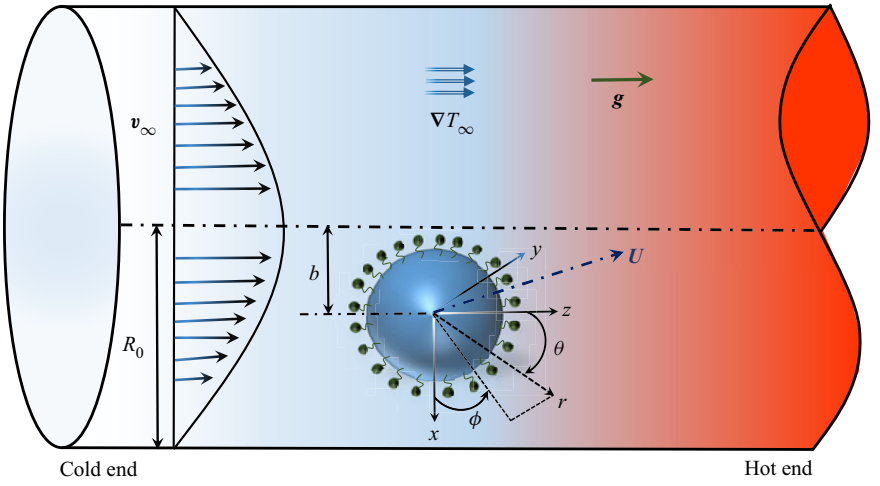

Figure 3. Schematic of a Poiseuille flow (as a special case of the Stokes flow) in a cylinder of radius R_0 in which a surfactant-laden droplet is released at a distance b from the axis. Thermal gradient and gravity in the streamwise direction. Other notation is similar to figure 1.

is discussed in detail. Accordingly, in this limit, due to the resistive behaviour of the surfactant molecules, the surface of the drop becomes completely immobilized. This is referred as a two-dimensional incompressible surface. Stone & Masoud (2015) have shown that this incompressible surface induces the subphase fluid to flow in planes parallel to the interface. As a result, this creates a large velocity gradient and enhances the drag compared to a clean interface (no surfactant). By looking into the first two terms in (3.11), we can infer that $(3\mu + 2)/3(\mu + 1)$ and $\mu/(\mu + 1)$ are less than unity. Hence the drag experienced by the droplet in the large Ma_Γ limit is more compared to that of a droplet with a clean interface.

The first-order drag $\boldsymbol{D}_1^H$ and droplet velocity $\boldsymbol{U}_1$ are given by

$$\boldsymbol{D}_1^H = -6\pi \boldsymbol{U}_1 + 2\pi \boldsymbol{Z}_1, \quad \text{and} \quad \boldsymbol{U}_1 = \tfrac{1}{3}\boldsymbol{Z}_1 + \boldsymbol{U}_{B,1}, \tag{3.20a,b}$$

where the complete expression for $\boldsymbol{Z}_1$ is given in (A13).

4. Results and discussion

In the preceding section, we covered the general approach for solving an arbitrary Stokes flow. In this section, we investigate a surfactant-laden droplet in a Poiseuille flow as a special case (see figure 3). The Poiseuille flow $\boldsymbol{v}_\infty = (0, 0, V_z)$ experienced by the droplet is described in the form (Pak *et al.* 2014)

$$V_z = 1 - \left(\frac{r}{R_0}\right)^2 \sin^2\theta - \left(\frac{b}{R_0}\right)^2 - \frac{2rb}{R_0^2}\sin\theta\cos\phi. \tag{4.1}$$

Here, the parameter b represents the distance between the centre of the droplet and the centreline of the flow, and R_0 is the radius of the pipe. For the chosen velocity field (4.1),

the associated scalars that describe the far-field conditions are

$$A_\infty = \left[\frac{r}{2}\left(1-\frac{b^2}{R_0^2}\right)-\frac{r^3}{5R_0^2}\right]P_1^0(\cos\theta)+\left(\frac{r^3}{30R_0^2}\right)P_3^0(\cos\theta)+\left(\frac{br^2}{9R_0^2}\right)P_2^1(\cos\theta)\cos\phi, \tag{4.2a}$$

$$B_\infty = \left(\frac{br}{R_0^2}\right)P_1^1(\cos\theta)\sin\phi. \tag{4.2b}$$

4.1. *Temperature distribution*

In figure 4, we have shown temperature isosurfaces on the droplet at $r = 1$. The meridional coordinate θ is measured along the droplet surface starting from the downstream ($\theta = 0$) to the upstream ($\theta = \pi$) location. In the absence of a far-field temperature gradient ($G = 0$), we observe that a centred monopole generates a uniform temperature on the droplet surface (see figure 4*a*). For the singularity strength $S = 2$, we observe the uniform temperature equal to a value 2. With the presence of ambient gradient ($G = 1$), the surface temperature varies, and it is different from a uniform value (see figure 4*b*). These variations occur primarily due to the surrounding thermal gradient and not due to the internal thermal singularity.

In the case of an off-centred monopole (with $r = 0.5$, $\theta = 0$, $\phi = 0$), the temperature is maximum at $\theta = 0$ and minimum at $\theta = \pi$ (see figures 4*c*,*d*). A similar behaviour is also seen for a dipole oriented in the streamwise direction (see figures 4*f*,*g*). However, in the case of a dipole oriented perpendicular to the flow, the maximum surface temperature is observed at $\theta = \pi/2$ for $G = 0$ (see figure 4*h*), and in a direction different from the streamwise and transverse directions for $G \neq 0$ (see figure 4*i*). We have quantified $T(r = 1, \theta, \phi = 0)$ for the presence of a monopole and a dipole in figures 4(*e*) and 4(*j*), respectively. Note that the temperature variation on the droplet surface results in additional thermal Marangoni stress due to singularities, and thus affects the droplet migration.

4.2. *In the small-Pe_s limit ($Pe_s \ll 1$)*

For $Pe_s \ll 1$, we have computed surfactant concentration (using (A4) and (A8) in Appendix A), the drag and the droplet migration velocity (see Appendix B). Our generalized calculations match with Pak *et al.* (2014) in the absence of ambient thermal field ($G = 0$) and internal thermal singularities. Even in the presence of thermocapillary effects (without any singularities), our results agree with Das *et al.* (2018) and Sharanya *et al.* (2019). In the following two subsubsections, we discuss both surfactant distribution and droplet velocity in the presence of thermal singularities.

4.2.1. *Surfactant distribution*

The surfactant distribution $\Gamma(\theta, \phi)$ for a droplet released on a Poiseuille flow axis ($b = 0$) is shown in figure 5 for different thermal singularities. Here, the ambient thermal field is acting along the imposed Poiseuille flow. The surfactant distribution is relatively high at $\theta = \pi$ (west) compared to $\theta = 0$ (east), and the observed is due to the Marangoni stress-induced flow on the droplet surface. Interestingly, the east–west located surfactant distribution moves towards the north–south directions when a dipole is oriented in the cross-stream directions, so we observe surfactant accumulation at the south-west region

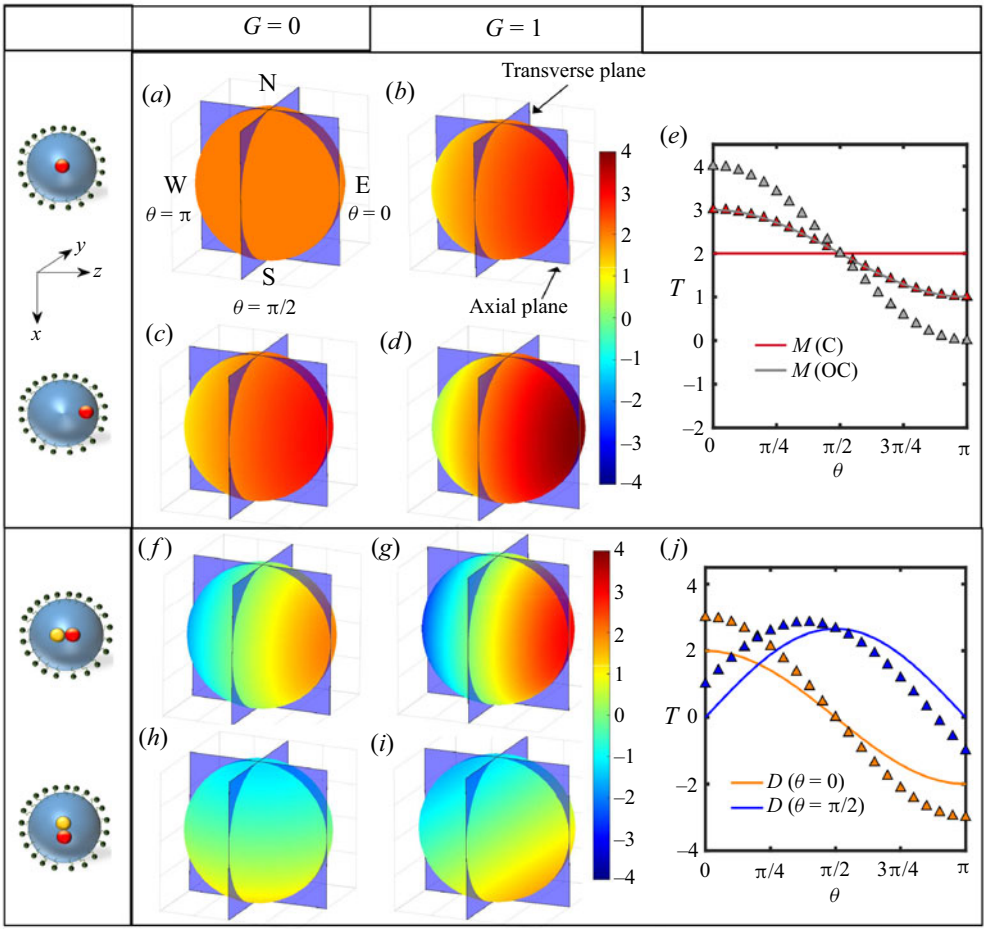

Figure 4. Temperature (T) contours on the droplet surface for two ambient thermal gradients $G = 0$ and 1. Droplets with (a–d) monopole-based, and (f–i) dipole-based thermal singularities. On the droplet surface, the θ direction begins at east (E) and ends at north (N) in the clockwise direction covering south (S) and west (W) points. The droplet is subjected to ambient flow experienced as downstream at $\theta = 0$ and upstream at $\theta = \pi$. (e,j) Temperature profiles in the θ direction for fixed $\phi = 0$. Continuous lines for $G = 0$, and triangles for $G = 1$. Red for centred (C) monopole, grey for off-centred (OC) monopole, orange for dipole oriented in the streamwise direction, and blue for dipole oriented in the cross-stream direction. Parameters are $S = 2$, $\kappa = 1$. Note that the temperature profiles are independent of other parameters such as droplet offset location from the axis b, Pe_s, μ, Ma_T, Ma_Γ and others.

of the droplet. A similar result, but an increase in non-uniform surfactant distribution, is found when the droplet is released at an offset from the flow centreline ($b \neq 0$).

4.2.2. *Droplet migration velocity*

In figure 6(a), we have shown the migration speed $|U_z|$ in the streamwise direction as a function of singularity strength S. In the absence of thermal singularity ($S = 0$), we found $|U_z| \approx 1.05$, which agrees with the results of Das *et al.* (2018) for the chosen parameters. A centred monopole does not affect the migration speed (refer to (B2)), which matches the results of Rednikov & Ryazantsev (1989) for homogeneous internal heating of a droplet. For $S > 0$, the speed increases above 1.05 for both the off-centred monopole and

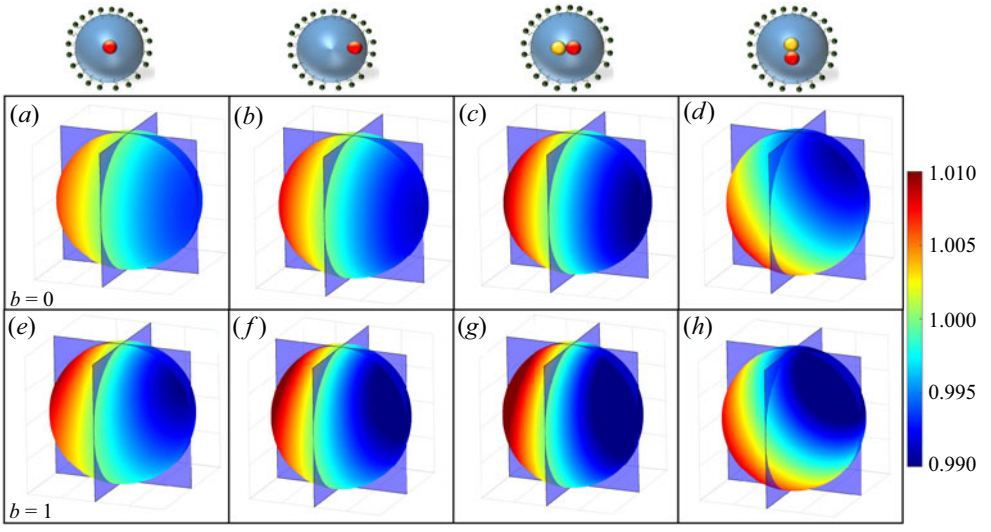

Figure 5. Surfactant concentration Γ on the droplet surface in the presence of (*a*,*e*) a centred monopole, (*b*,*f*) an off-centred monopole, (*c*,*g*) a dipole oriented in the streamwise direction, and (*d*,*h*) a dipole oriented in the cross-stream direction. Droplet released on flow centreline/axis ($b = 0$) from (*a*) to (*d*), and released at an offset from the flow axis ($b = 1$) from (*e*) to (*h*). Colour bar for Γ in a linear range from 0.99 (blue) to 1.01 (red). Parameters are $S = 2$, $Pe_s = 0.1$, $G = 1$, $Ma_T = 1$, $Ma_\Gamma = 10$, $\kappa = 1$, $\mu = 1$, $R_0 = 5$ and $Bo = 0$.

the dipole. In the inset of figure 6(*a*), we have shown $U_z/|U_z(S = 0)|$. The droplet with the dipole orientation $\theta = 0$ gives maximum speed compared to any other orientation. In figure 6(*b*), droplet cross-stream speed $|U_x|$ as a function of S is shown. Migration velocity increases with increasing S. Interestingly, we observe that a dipole can reverse the direction of the droplet migration when S is greater than a critical value S_c. In the inset of figure 6(*b*), we have shown the droplet's relative cross-stream velocity $U_x/|U_x(S = 0)|$. For small values of S, the relative speed is negative, which indicates that the drop migrates towards the flow centreline. With an increase in S, the droplet can migrate away from the centreline. At critical strength S_c, we find $U_x = 0$. It is worth noting that S_c is a function of the parameters μ, κ, Ma_T, Ma_Γ and dipole orientation angle θ. Figure 7 shows S_c as a function of the dipole orientation θ. We observe that S_c decreases by nearly two orders of magnitude when orientation changes from $\theta = 0$ to $\pi/2$ with a small variation in Ma_T. This suggests that when the dipole is oriented in the cross-stream direction ($\theta = \pi/2$), a small S is sufficient to perturb the droplet motion from the centreline to away from it. In the insets of figure 7, we have shown S_c dependence on μ (figure 7*a*) and κ (figure 7*b*). We observe that S_c decreases with both μ and κ; however, we find that κ dependence corresponds to a significant change in S_c.

4.3. *Small-Pe_s versus large-Pe_s limits*

The migration velocity of a surfactant-laden droplet (subjected to a streamwise oriented dipole) in the large-Pe_s limit is given by

$$\boldsymbol{U} = \left[1 - \frac{2}{3R_0^2} - \frac{b^2}{R_0^2} + \frac{2\omega}{9}\frac{Bo}{Ca}\right]\hat{k} - Ma_\Gamma^{-1}\left[\frac{(G + \kappa S)b\,Ma_T}{(\kappa + 2)R_0^2} + \frac{2b}{3R_0^4} + \frac{\omega b}{9R_0^2}\frac{Bo}{Ca}\right]\hat{i} + O(Ma_\Gamma^{-1}). \tag{4.3}$$

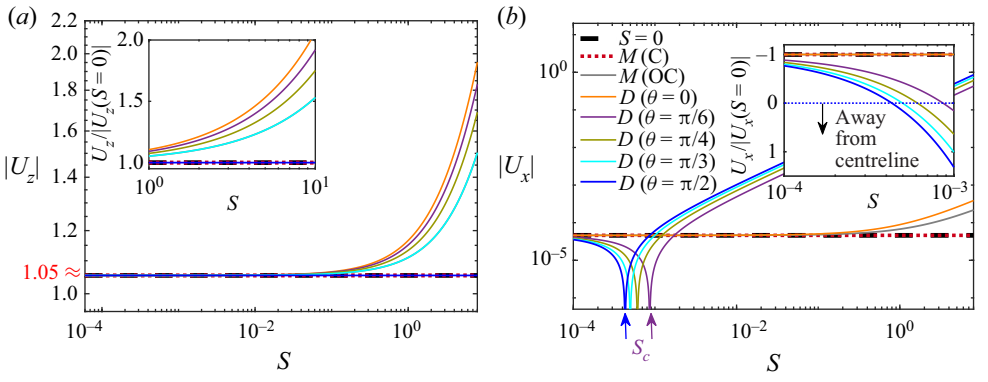

Figure 6. Droplet velocity (in magnitude) as a function of thermal singularity strength S: (*a*) streamwise direction, and (*b*) cross-stream direction. Thick dashed line for the absence of thermal singularity, centred monopole (red dashes) and off-centred monopole (grey line). Dipole with different orientations in continuous lines: $\theta = 0$ (orange), $\pi/6$ (violet), $\pi/4$ (green), $\pi/3$ (cyan) and $\pi/2$ (blue). Insets for droplet velocity re-scaled (or compared) by the case with no thermal singularity. Note that the droplet moves away from the centreline (or axis) beyond critical singularity strength S_c (defined for a dipole). Parameters are $Pe_s = 0.1$, $G = 1$, $b = 1$, $Ma_T = 1$, $Ma_\Gamma = 10$, $\kappa = 1$, $\mu = 1$, $R_0 = 5$ and $Bo = 0$. Here, $S = 0$ corresponds to no thermal singularity (Das *et al.* 2018).

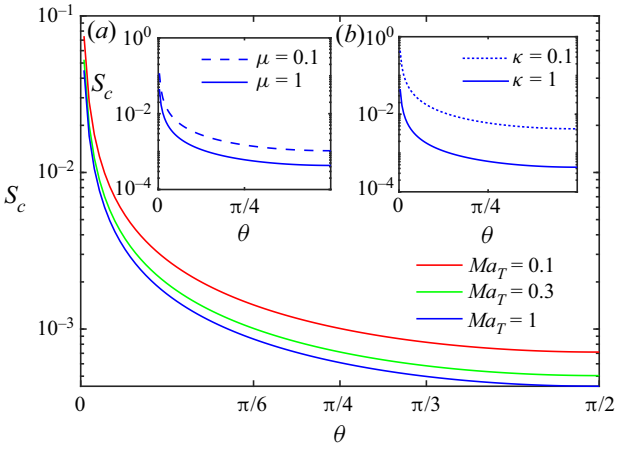

Figure 7. Critical dipole strength S_c as a function of dipole orientation angle θ for $Ma_T = 0.1$ (red), $Ma_T = 0.3$ (green), and $Ma_T = 1$ (blue). Parameters are $Pe_s = 0.1$, $G = 1$, $Ma_\Gamma = 10$, $\kappa = 1$, $\mu = 1$, $R_0 = 5$ and $Bo = 0$. Insets for different (*a*) viscosity and (*b*) thermal conductivity.

In figure 8, we have presented the results for both small- and large-Pe_s limits. Notably, we can observe that the magnitude of the cross-stream migration velocity is approximately one order higher in the large-Pe_s limit compared to the small-Pe_s limit. The behaviour remains consistent for other thermal singularities as well.

4.4. *A discussion on critical Marangoni number set by thermal singularities for small Pe_s*

In the earlier sections, we have constructed a generalized result on surfactant-laden droplet motion and its control using thermal singularities. Here, we present an overview of the role played by thermocapillary action and surfactants on droplet motion.

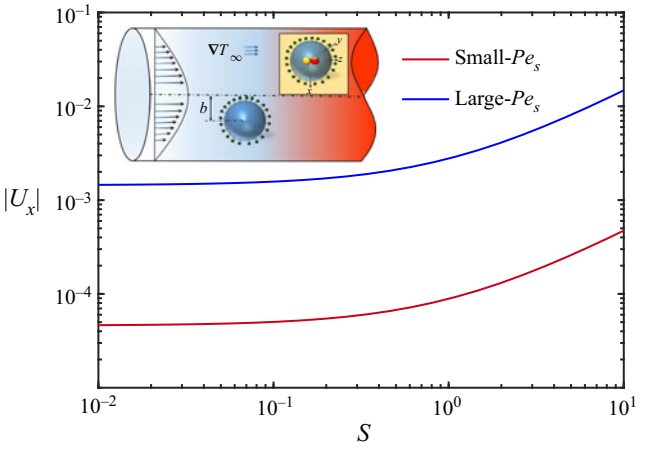

Figure 8. Cross-stream velocity (in magnitude) as a function of singularity strength S under small-Pe_s (red) and large-Pe_s (blue) limits. Parameters are $Pe_s = 0.1$, $G = 1$, $Ma_T = 1$, $Ma_\Gamma = 10$, $\kappa = 1$, $\mu = 1$, $R_0 = 5$ and $Bo = 0$.

In the case of droplet-based microfluidics, surfactants are added to the continuous or dispersed phase to maintain the stability of the droplet, prevent coalescence and avoid any cross-contamination. However, such addition of surfactant leads to a reduction in droplet speed at first order in the streamwise direction without any cross-stream migration, and a cross-stream migration towards the Poiseuille flow centreline is seen as a second-order effect in Pe_s (Pak *et al.* 2014). The stabilized droplet that reaches the centreline may control the overall production rate in micro-devices. Note that this technique, with precise control, can be highly advantageous in cell processing applications, optimizing bioreactor efficiency, etc. Now, if we can disperse the droplets from the centreline and at the same time maintain stability, then we can account for more droplets in the device, thus improving the overall production rate. Similarly, an imposed thermal gradient (without any surfactants) results in a leading-order effect in droplet streamwise motion either by speeding up (if the thermal gradient aligns with the flow) or slowing down (if the thermal gradient opposes the flow) without any cross-stream movement. Although manipulating droplet speed is possible, this approach does not achieve a high droplet production rate within a limited device width. An alternative control mechanism that manipulates droplet migration efficiency would be advantageous. In this regard, a thermal singularity helps to control the droplet motion with leading-, first- and second-order effects in the streamwise and cross-streamwise directions. For example, a dipole can help the droplet to speed up or slow down, depending on its orientation.

In this context, we seek whether a critical Marangoni number ($Ma^*_{T,z}$ or $Ma^*_{\Gamma,z}$) exists at which a droplet halts ($U_z = 0$) or reverses its motion. Our focus in this subsection is solely on the streamwise migration velocity of the droplet. The reason behind this emphasis is that it is more feasible to maintain a thermal gradient in the streamwise direction due to the device configurations, instead of in the cross-stream direction. Furthermore, we are interested in exploring the interfacial tension effects, thus neglecting gravity ($Bo = 0$) for the discussion. In the following, we show four cases: (1) when thermal gradient alone is present, without surfactant or the singularities ($Ma_T \neq 0$, $Ma_\Gamma = 0$ and $S = 0$); (2) when surfactant alone is present, without thermal gradient or the singularities ($Ma_T = 0$, $Ma_\Gamma \neq 0$ and $S = 0$); (3) when both thermal gradients and surfactant are present, but

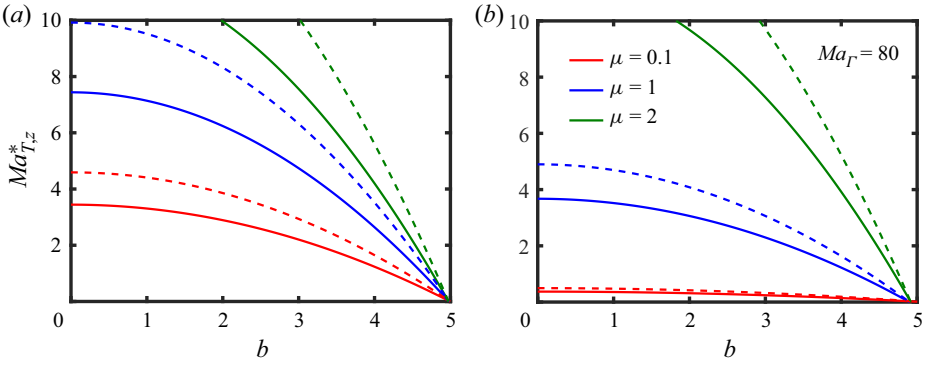

Figure 9. Critical Marangoni number required to halt droplet released at an offset distance b in a Poiseuille flow: (a) for case1, and (b) for case 3. Continuous lines for $\kappa = 1$ and dashed lines for $\kappa = 2$. Other parameters are $G = -1$ and $R_0 = 5$.

thermal singularity is absent ($Ma_T \neq 0$, $Ma_\Gamma \neq 0$ and $S = 0$); and (4) when thermal gradients, surfactant and the singularities are present ($Ma_T \neq 0$, $Ma_\Gamma \neq 0$ and $S \neq 0$). Note that in all the cases, the applied thermal gradient is opposite to the flow direction (i.e. $G = -1$) with a specific aim of halting a droplet's motion.

4.4.1. *Case 1: $Ma_T \neq 0$, $Ma_\Gamma = 0$ and $S = 0$*

We have equated $U_z = 0$ (refer to (B2)) and found the critical thermal Marangoni number as

$$Ma^*_{T,z} = -\frac{(3\mu + 2)(\kappa + 2)}{2G}\left[1 - \left(\frac{b}{R_0}\right)^2\right] + \frac{\mu(\kappa + 2)}{2GR_0^2}. \tag{4.4}$$

In figure 9(a), we have shown $Ma^*_{T,z}$ as a function of droplet offset distance b for different values of μ. A droplet away from the centreline requires small $Ma^*_{T,z}$ to cease its motion. For highly viscous droplets, a higher thermal gradient is needed to cease the droplet. The high thermal conductivity of the droplet corresponds to low thermocapillary stresses on the interfaces, which results in a large $Ma^*_{T,z}$.

4.4.2. *Case 2: $Ma_T = 0$, $Ma_\Gamma \neq 0$ and $S = 0$*

The critical surfactant Marangoni number $Ma^*_{\Gamma,z}$ can be found from the equation

$$1 - \left(\frac{b}{R_0}\right)^2 - \frac{2\mu}{(3\mu + 2)R_0^2} - \frac{4\,Pe_s}{3(3\mu + 2)^2 R_0^2} Ma^*_{\Gamma,z} + \frac{4\,Pe_s^2}{3(3\mu + 2)^3 R_0^2}(Ma^*_{\Gamma,z})^2 = 0. \tag{4.5}$$

Note that this is a quadratic equation in terms of $Ma^*_{\Gamma,z}$. In order to obtain a real non-zero solution, the discriminant should be positive. Consequently, simplifying the discriminant of (4.5) yields the condition $0 < R_0^2 - b^2 < (6\mu + 1)/(3\mu + 2)$. Thus we can infer that unless the droplet is released very close to the wall (i.e. $b \approx R_0$), surfactants can indeed reduce the streamwise migration velocity of the droplet, but they cannot bring it to halt completely.

4.4.3. *Case 3: $Ma_T \neq 0$, $Ma_\Gamma \neq 0$ and $S = 0$*
We found the critical thermal Marangoni number as (using (B2))

$$Ma^*_{T,z} = \frac{(\kappa+2)[3(b^2-R_0^2)(3\mu+2)^3 + 6\mu(3\mu+2)^2 + 4\,Ma_\Gamma\,(3\mu+2)\,Pe_s - 4\,Ma_\Gamma^2\,Pe_s^2]}{6GR_0^2[(3\mu+2)^2 - Ma_\Gamma\,(3\mu+2)\,Pe_s + Ma_\Gamma^2\,Pe_s^2]}. \tag{4.6}$$

In figure 9(*b*), we have shown $Ma^*_{T,z}$ as a function of b. As mentioned earlier, the presence of surfactant reduces the droplet speed, and a tiny opposing thermal gradient is enough to halt the droplet completely (compare the $\mu = 1$ line in figures 9*a*,*b*), thereby reducing the critical Ma_T required.

In figure 10, we have shown the variation of $Ma^*_{T,z}$ as a function of Ma_Γ. For a droplet released either on the centreline or near the walls in a Poiseuille flow, surprisingly, our result reveals that we need larger thermal gradients (or large critical $Ma^*_{T,z}$) for $Ma_\Gamma < 20$. Note that (4.6) has two asymptotic limits in terms of small and large values of $Ma_\Gamma Pe_s$. For smaller values, we have

$$Ma^*_{T,z}\big|_{Ma_\Gamma Pe_s \to 0} \approx \left(\frac{\kappa+2}{6GR_0^2}\right)[6\mu + 3(3\mu+2)(b^2-R_0^2) + \{2+3(b^2-R_0^2)\}\,Ma_\Gamma\,Pe_s], \tag{4.7}$$

which is a linearly increasing function of $Ma_\Gamma\,Pe_s$. In the case of large $Ma_\Gamma Pe_s$, we find

$$Ma^*_{T,z}\big|_{Ma_\Gamma Pe_s \to \infty} \approx -\frac{4(\kappa+2)}{6GR_0^2(3\mu+2)^2}\left[1 - \frac{1}{(Ma_\Gamma\,Pe_s)^2}\left(1 + (3\mu+2)^3\left(\frac{1}{2} + \frac{3(b^2-R_0^2)}{4}\right)\right)\right]. \tag{4.8}$$

Both the asymptotic limits are shown in figure 10. Interestingly, at leading order, the small $Ma_\Gamma Pe_s$ limit depends on b, whereas at the large limit, it does not. Note that the large limit is non-zero and has a finite positive value close to zero. The peak values observed on critical $Ma^*_{T,z}$ curves near $Ma_\Gamma \approx 20$ decrease with increasing b.

4.4.4. *Case 4: $Ma_T \neq 0$, $Ma_\Gamma \neq 0$ and $S \neq 0$*
In the case of thermal singularities, we have generalized $Ma^*_{T,z}$ as a function of Ma_Γ and S using (B6) for a dipole oriented along ($\theta = 0$) or opposite to ($\theta = \pi$) the streamwise direction. The corresponding equations for $Ma^*_{T,z}$ are given by

$$Ma^*_{T,z} = \frac{(\kappa+2)[3(b^2-R_0^2)(3\mu+2)^3 + 6\mu(3\mu+2)^2 + 4\,Ma_\Gamma\,(3\mu+2)\,Pe_s - 4\,Ma_\Gamma^2\,Pe_s^2]}{6(G+\kappa S)R_0^2[(3\mu+2)^2 - Ma_\Gamma\,(3\mu+2)\,Pe_s + Ma_\Gamma^2\,Pe_s^2]} \tag{4.9}$$

and

$$Ma^*_{T,z} = \frac{(\kappa+2)[3(b^2-R_0^2)(3\mu+2)^3 + 6\mu(3\mu+2)^2 + 4\,Ma_\Gamma\,(3\mu+2)\,Pe_s - 4\,Ma_\Gamma^2\,Pe_s^2]}{6(G-\kappa S)R_0^2[(3\mu+2)^2 - Ma_\Gamma\,(3\mu+2)\,Pe_s + Ma_\Gamma^2\,Pe_s^2]}, \tag{4.10}$$

respectively. Note that the mentioned equations are similar to (4.6), except that the term G in the denominator is replaced by $G \pm \kappa S$. For a dipole oriented in the flow direction, the required critical value can reach infinity if $G + \kappa S \to 0$ (since $G = -1$). In contrast,

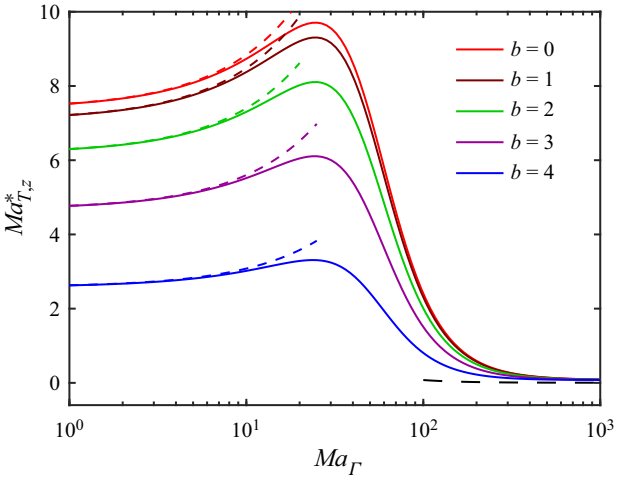

Figure 10. Critical thermal Marangoni number $Ma^*_{T,z}$ as a function of Ma_Γ for case 3. Low Ma_Γ follows (4.7) (thin dashed lines at different b), and large Ma_Γ follows (4.8) (thick dashed line). Parameters are $\mu = 1$, $\kappa = 1$, $Pe_s = 0.1$, $G = -1$, $R_0 = 5$ and $Bo = 0$.

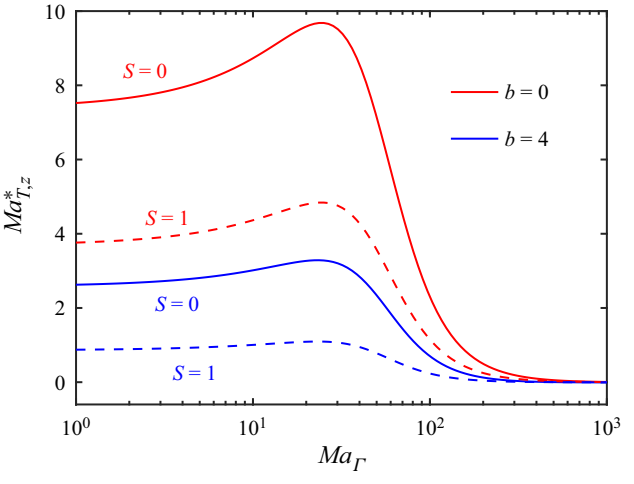

Figure 11. Critical thermal Marangoni number $Ma^*_{T,z}$ as a function of Ma_Γ for a dipole with different strengths S oriented opposite to the streamwise direction (case 4). Other parameters are $\mu = 1$, $\kappa = 1$, $Pe_s = 0.1$, $G = -1$, $R_0 = 5$ and $Bo = 0$.

for a dipole oriented opposite to the flow, the denominator (in magnitude) increases with an increase in S, thus the required critical Marangoni number decreases (see figure 11). Note that the functional form and the asymptotic behaviour in case 4 remain the same, as mentioned in case 3.

4.5. *Dependency on viscosity ratio in the small-Pe_s limit*

Analysing droplet migration in terms of viscosity ratio in microfluidics is crucial for understanding and optimizing microfluidic systems (Baumgartner, Brenn & Planchette 2020). In this context, we have shown U_z and U_x as functions of μ (refer to (B6) in Appendix B) in figure 12. For a fixed μ, U_z for a centred monopole and dipole (oriented

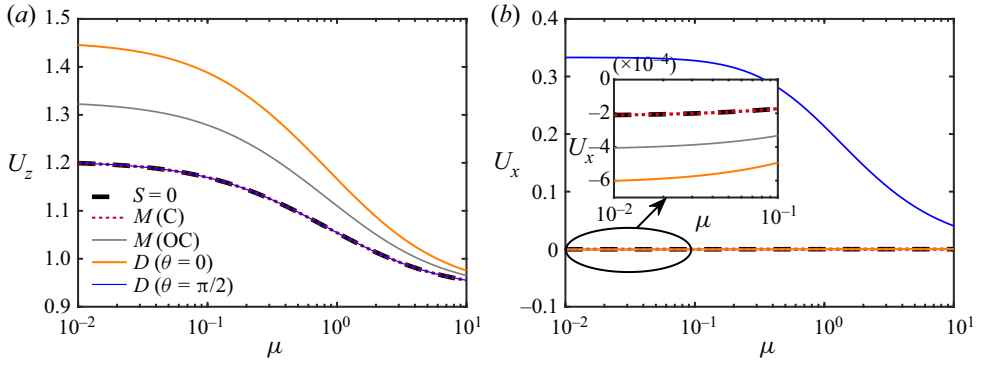

Figure 12. Droplet migration velocity (*a*) streamwise (U_z) and (*b*) cross-stream (U_x) versus viscosity ratio μ for $S = 0$ (dashed line), centred monopole (dotted line), off-centred monopole (grey), dipole oriented streamwise (orange) and dipole oriented transversely (blue). The ambient thermal field acts along the imposed Poiseuille flow, i.e. $G = 1$. Other parameters are $S = 2$, $Ma_T = 1$, $Ma_\Gamma = 10$, $Pe_s = 0.1$, $\kappa = 1$, $b = 1$, $R_0 = 5$ and $Bo = 0$.

perpendicular to the flow) coincides with the case without any thermal singularity, and matches the results of Das *et al.* (2018) for the chosen parameter values. Both the off-centred monopole and streamwise oriented dipole increase the migration velocity. For a small viscosity ratio ($\mu = 0.01$), U_z is increased by approximately 10 % for an off-centred monopole, and by 25 % for a streamwise oriented dipole when compared to no thermal singularity (Das *et al.* 2018). However, a cross-stream oriented dipole does not affect U_z. For large μ, the droplet behaves as a rigid sphere, and the corresponding influence of the Marangoni stress becomes insignificant, resulting in a decrease in U_z. In figure 12(*b*), we have shown U_x as a function of μ. We can observe that the cross-stream migration velocity is influenced significantly by a transversely oriented ($\theta = \pi/2$) dipole in comparison to other singularities.

It is worth mentioning that when considering a centred/off-centred monopole and a streamwise oriented dipole, the cross-stream migration velocity appears at $O(Pe_s^2)$. However, in the case of a transversely oriented dipole, the cross-stream migration velocity can be observed from $O(1)$ onwards. Further, in this particular configuration (droplet with transversely oriented dipole), the leading-order cross-stream migration is due mainly to the thermocapillary effect (refer to (B6)). From $O(Pe_s)$ onwards, the effect of surfactant can be seen (refer to figure 13*a*), which is different from the earlier $O(Pe_s^2)$ corrections (Das *et al.* 2018). This is due to the coupling between the thermal and the surfactant-induced Marangoni stresses. Even for a very small singularity strength ($S = 2 \times 10^{-4}$), the leading-order effect can be observed very clearly. In figure 13(*b*), we classify the regimes with reference to the migration of the droplet. Accordingly, for a specific (Ma_Γ, Ma_T) pair, one can identify whether the droplet migrates away from or towards the centreline when the other parameters are fixed.

5. Summary and conclusions

In this paper, we have analysed the migration of a droplet in an arbitrary Stokes flow under the influence of thermocapillary and surfactant-induced Marangoni stress for different types of internal thermal singularities. Neglecting the effects of thermal convection, fluid inertia and shape deformation, we have obtained analytical expressions for the temperature

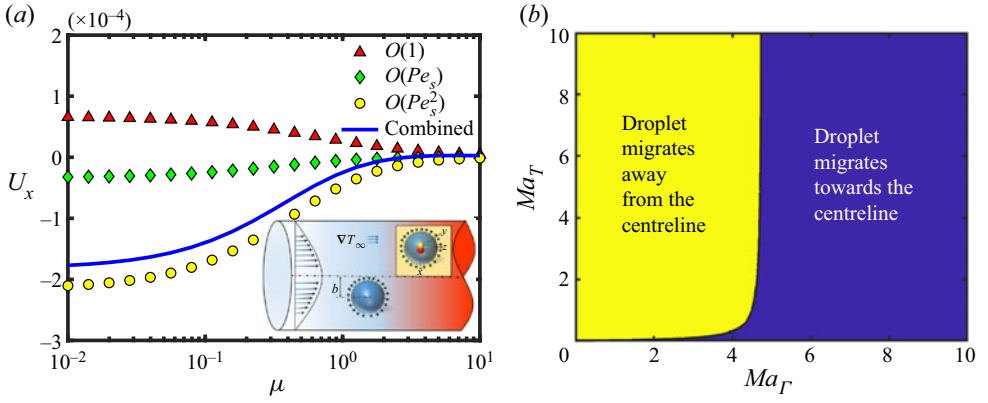

Figure 13. (*a*) Droplet's cross-stream migration velocity U_x versus viscosity ratio μ for a transversely oriented dipole. Migration velocity for different orders: leading order (triangles), first order (diamonds), second order (circles) and combined (continuous line). Here, $Ma_T = 1$ and $Ma_\Gamma = 10$. (*b*) Regime diagram showing two different patterns of droplet cross-stream motion for $\mu = 1$. Other parameters are $S = 2 \times 10^{-4}$, $G = 1$, $Pe_s = 0.1$, $\kappa = 1$, $b = 1$, $R_0 = 5$ and $Bo = 0$.

field, surfactant concentration and migration velocity using perturbation analysis for the two limiting cases: (i) $Pe_s \ll 1$, in which surface diffusion dominates the surfactant transport; and (ii) $Pe_s \gg 1$, in which surface convection dominates the surfactant transport. The migration velocity of a surfactant-laden droplet in an ambient Poiseuille flow (as a particular case of an arbitrary Stokes flow) depends strongly upon the type of internal thermal singularity considered. The migration velocity is unaffected by a localized centred monopole heat source, similar to the findings for a droplet subjected to homogeneous internal heating by Rednikov & Ryazantsev (1989). However, an off-centred monopole or a dipole heat source influences the overall migration of the droplet.

Our analytical results show that in the small-Pe_s limit, a drop with an off-centred monopole or a streamwise oriented ($\theta = 0$) dipole experiences cross-stream migration at $O(Pe_s^2)$. The effect becomes prominent in the case of an oriented dipole ($\theta \neq 0$). In this scenario, we observe the cross-stream migration at the leading order, which is due purely to the thermocapillary effects generated by the asymmetric temperature distribution on the droplet surface. Due to the coupling between thermocapillary-induced Marangoni stress and surfactant-induced Marangoni stress, the combined effect is observed at $O(Pe_s)$ onwards, which is different from the classical $O(Pe_s^2)$ findings by Das *et al.* (2018). Furthermore, when the droplet is positioned at the flow centreline, it can also move across the stream with this configuration. As we increase the strength of thermal singularity, the migration velocity of the droplet gets enhanced. Remarkably, in the presence of an oriented dipole, a critical strength S_c exists that determines whether the droplet migrates towards or away from the flow centreline. Further, in the absence of a thermal gradient (due to both ambient temperature as well as thermal singularity), surfactants can reduce the droplet migration velocity, but they are unable to halt it completely unless the droplet is close enough to the wall. However, when both the thermal gradient and surfactants are present, we can easily bring the droplet to a complete halt by applying a dipole oriented opposite to the flow. In comparison to the small-Pe_s limit, the magnitude of the cross-stream migration velocity is approximately one order higher for large Pe_s.

In summary, we have developed a general methodology for addressing thermal singularities in droplet dynamics, and provided Faxen's laws for drag and

migration velocity. Our research findings indicate that thermal singularities have the potential to control both the streamwise and cross-stream migration velocities of surfactant-laden droplets. The analytical results obtained in this study serve as valuable benchmarks for future computational methods pertaining to droplet dynamics. For future scope, our findings provide essential insights for estimating drag and energy requirements in microbe-encapsulated droplet technologies, thus opening up promising avenues for further exploration in this field.

Acknowledgements. The authors would like to acknowledge Professor S. Chakraborty, Department of Mechanical Engineering, Indian Institute of Technology (IIT) Kharagpur, for his insightful suggestions.

Funding. A.B. gratefully acknowledges the research support from the Council of Scientific & Industrial Research (CSIR), Government of India. R.L. acknowledges research grants from the Board of Research and Nuclear Sciences (BRNS) and the Mathematical Research Impact Centric Support (MATRICS) scheme sponsored by the Government of India to study multiphase flows. We sincerely thank P. Shakti for computing resources developed under National Super Computing Mission at IIT Kharagpur, India.

Declaration of interests. The authors report no conflict of interest.

Author ORCIDs.
Arindam Basak https://orcid.org/0000-0002-5567-4403;
Rajaram Lakkaraju https://orcid.org/0000-0002-1968-820X;
G.P. Raja Sekhar https://orcid.org/0000-0001-9147-4030.

Appendix A. Drag and migration velocity in the small- and large-Pe_s limits

We have considered a Cartesian coordinate system (x, y, z) having its origin at the droplet centre, as shown in figure 1. We are interested in calculating the axial and cross-stream migration velocity in this frame of reference (Subramanian & Balasubramaniam 2001).

A.1. *For* $Pe_s \ll 1$

The leading-order drag, as given in (3.11), is

$$\boldsymbol{D}_0^H = 6\pi \left(\frac{3\mu+2}{3(\mu+1)} [\boldsymbol{u}_{\infty,0}]_0 + \frac{\mu}{6(\mu+1)} [\nabla^2 \boldsymbol{u}_{\infty,0}]_0 + \frac{2\,Ma_T}{3(\mu+1)(\kappa+2)} [\nabla T_\infty]_0 + \frac{2\kappa \mathscr{b}_1\, Ma_T}{3(\mu+1)(\kappa+2)} \boldsymbol{Y}_0 \right). \tag{A1}$$

The aforementioned compact forms are due to the relationships

$$\left.\begin{aligned} [\boldsymbol{u}_{\infty,\boldsymbol{0}}]_0 &= 2\alpha_1^{\infty(0)} (C_{11}^{(0)} \hat{i} + D_{11}^{(0)} \hat{j} + C_{10}^{(0)} \hat{k}), \\ [\nabla^2 \boldsymbol{u}_{\infty,\boldsymbol{0}}]_0 &= 20\hat{\alpha}_1^{\infty(0)} (C_{11}^{(0)} \hat{i} + D_{11}^{(0)} \hat{j} + C_{10}^{(0)} \hat{k}), \\ [\nabla T_\infty]_0 &= \mathscr{c}_1 (A_{11} \hat{i} + B_{11} \hat{j} + A_{10} \hat{k}). \end{aligned}\right\} \tag{A2}$$

Note that the vector

$$\boldsymbol{Y}_0 = A_{11} \hat{i} + B_{11} \hat{j} + A_{10} \hat{k} \tag{A3}$$

is related to the spherical harmonic $\mathcal{S}_n(\theta, \phi) = \sum_{m=0}^{n} P_n^m(\cos\theta)\,(A_{nm} \cos m\phi + B_{nm} \sin m\phi)$.

Now, using leading-order solutions, we solve the first-order surfactant transport equation given by (3.10*b*). We express the surfactant concentration Γ_1 in terms of surface spherical harmonics as

$$\Gamma_1 = \sum_{n=1}^{\infty}\sum_{m=0}^{n}\left(I_{nm}^{(1)}\cos m\phi + J_{nm}^{(1)}\sin m\phi\right)P_n^m(\cos\theta), \tag{A4}$$

where $I_{nm}^{(1)}$ and $J_{nm}^{(1)}$ are

$$I_{nm}^{(1)} = -\frac{(2n+1)(n-m)!}{2(n+m)!}\frac{1}{\pi n(n+1)}\int_{\phi=0}^{2\pi}\int_{\theta=0}^{\pi}(\nabla_s\cdot\boldsymbol{u}_{s,0})\,P_n^m(\cos\theta)\cos m\phi\sin\theta\,\mathrm{d}\theta\,\mathrm{d}\phi, \tag{A5a}$$

$$J_{nm}^{(1)} = -\frac{(2n+1)(n-m)!}{2(n+m)!}\frac{1}{\pi n(n+1)}\int_{\phi=0}^{2\pi}\int_{\theta=0}^{\pi}(\nabla_s\cdot\boldsymbol{u}_{s,0})\,P_n^m(\cos\theta)\sin m\phi\sin\theta\,\mathrm{d}\theta\,\mathrm{d}\phi, \tag{A5b}$$

which implies

$$I_{nm}^{(1)} = \left(\frac{2n-1}{\mu+1}\alpha_n^{\infty(0)} + \frac{2n+3}{\mu+1}\hat{\alpha}_n^{\infty(0)}\right)C_{nm}^{(0)} - \frac{(\mathscr{c}_n+\kappa\mathscr{b}_n)\,Ma_T}{(\mu+1)(n\kappa+n+1)}A_{nm}, \tag{A6a}$$

$$J_{nm}^{(1)} = \left(\frac{2n-1}{\mu+1}\alpha_n^{\infty(0)} + \frac{2n+3}{\mu+1}\hat{\alpha}_n^{\infty(0)}\right)D_{nm}^{(0)} - \frac{(\mathscr{c}_n+\kappa\mathscr{b}_n)\,Ma_T}{(\mu+1)(n\kappa+n+1)}B_{nm}. \tag{A6b}$$

Similarly, the first-order hydrodynamic drag and corresponding migration velocity are given by (3.13*a*) and (3.13*b*), where

$$\boldsymbol{Y}_1 = I_{11}^{(1)}\hat{i} + J_{11}^{(1)}\hat{j} + I_{10}^{(1)}\hat{k}. \tag{A7}$$

Now, let us consider Γ_2 as

$$\Gamma_2 = \sum_{n=1}^{\infty}\sum_{m=0}^{n}(I_{nm}^{(2)}\cos m\phi + J_{nm}^{(2)}\sin m\phi)P_n^m(\cos\theta). \tag{A8}$$

Correspondingly, $I_{nm}^{(2)}$ and $J_{nm}^{(2)}$ are given by

$$I_{nm}^{(2)} = -\frac{(2n+1)(n-m)!}{2(n+m)!}\frac{1}{\pi n(n+1)} \times\int_{\phi=0}^{2\pi}\int_{\theta=0}^{\pi}(\nabla_s\cdot(\boldsymbol{u}_{s,0}\Gamma_1+\boldsymbol{u}_{s,1}\Gamma_0))P_n^m(\cos\theta)\cos m\phi\sin\theta\,\mathrm{d}\theta\,\mathrm{d}\phi, \tag{A9a}$$

$$J_{nm}^{(2)} = -\frac{(2n+1)(n-m)!}{2(n+m)!}\frac{1}{\pi n(n+1)} \times\int_{\phi=0}^{2\pi}\int_{\theta=0}^{\pi}(\nabla_s\cdot(\boldsymbol{u}_{s,0}\Gamma_1+\boldsymbol{u}_{s,1}\Gamma_0))P_n^m(\cos\theta)\sin m\phi\sin\theta\,\mathrm{d}\theta\,\mathrm{d}\phi. \tag{A9b}$$

The second-order hydrodynamic drag and migration velocity are given by (3.14*a*) and (3.14*b*). The corresponding compact form is

$$\boldsymbol{Y}_2 = I_{11}^{(2)}\hat{i} + J_{11}^{(2)}\hat{j} + I_{10}^{(2)}\hat{k}. \tag{A10}$$

A.2. *For $Pe_s \gg 1$*

For large Pe_s, the first-order surfactant concentration is given by

$$\Gamma_1 = \sum_{n=1}^{\infty}\sum_{m=0}^{n} \Lambda_n (C_{nm}^{(0)} \cos m\phi + D_{nm}^{(0)} \sin m\phi) P_n^m(\cos\theta), \tag{A11}$$

where

$$\Lambda_n = (2n-1)(2n+1)\alpha_n^{\infty(0)} + (2n+3)(2n+1)\hat{\alpha}_n^{\infty(0)} - \frac{(2n+1)(\mathscr{c}_n + \kappa \mathscr{b}_n)\, Ma_T}{(n\kappa + n + 1)}. \tag{A12}$$

Thus the first-order hydrodynamic drag and droplet migration velocity are given by (3.20*a*,*b*), where

$$\boldsymbol{Z}_1 = L_{111}\hat{i} + L_{112}\hat{j} + L_{101}\hat{k}, \tag{A13}$$

and the terms L_{nm1}, L_{nm2} are

$$L_{nm1} = -\frac{(2n+1)(n-m)!}{2\pi(n+m)!}\int_{\phi=0}^{2\pi}\int_{\theta=0}^{\pi} (\nabla_s \cdot \boldsymbol{u}_{s,0}) P_n^m(\cos\theta)\cos m\phi \sin\theta \,\mathrm{d}\theta\,\mathrm{d}\phi, \tag{A14a}$$

$$L_{nm2} = -\frac{(2n+1)(n-m)!}{2\pi(n+m)!}\int_{\phi=0}^{2\pi}\int_{\theta=0}^{\pi} (\nabla_s \cdot \boldsymbol{u}_{s,0}) P_n^m(\cos\theta)\sin m\phi \sin\theta \,\mathrm{d}\theta\,\mathrm{d}\phi. \tag{A14b}$$

Appendix B. Drag and migration velocity in Poiseuille flow for $Pe_s \ll 1$

Using the mentioned Poiseuille flow field (refer to (4.1)) and thermal conditions, we have computed the surfactant concentration Γ for different thermal singularities using (A4) and (A8). For a centred monopole, the surfactant concentration is given by

$$\begin{aligned}\Gamma = 1 &+ Pe_s\left[I_{10}^{(1)}\cos\theta + I_{21}^{(1)}\cos\phi\, P_2^1(\cos\theta) + I_{30}^{(1)}\, P_3^0(\cos\theta)\right] \\ &+ Pe_s^2\left[I_{10}^{(2)}\cos\theta + I_{21}^{(2)}\cos\phi\, P_2^1(\cos\theta) + I_{30}^{(2)}\, P_3^0(\cos\theta) + I_{11}^{(2)}\cos\phi\, P_1^1(\cos\theta)\right. \\ &\left. + I_{20}^{(2)}\, P_2^0(\cos\theta) + I_{22}^{(2)}\cos(2\phi)\, P_2^2(\cos\theta) + I_{31}^{(2)}\cos\phi\, P_3^1(\cos\theta)\right] + O(Pe_s^3),\end{aligned} \tag{B1}$$

where the quantities $I_{10}^{(1)}$, $I_{21}^{(1)}$, etc. are provided below. After evaluating (3.12), (3.13*a*), (3.13*b*), (3.14*a*) and (3.14*b*), we obtain the droplet migration velocity as

$$\begin{aligned}\boldsymbol{U} = &\left[1 - \left(\frac{b}{R_0}\right)^2 - \frac{2\mu}{(3\mu+2)R_0^2} + \frac{2G\, Ma_T}{(\kappa+2)(3\mu+2)} + \frac{2\omega}{3}\left(\frac{1+\mu}{3\mu+2}\right)\frac{Bo}{Ca}\right]\hat{k} + Pe_s\left[\frac{2}{3(3\mu+2)}\right. \\ &\left.\times\left(Ma_\Gamma\, I_{10}^{(1)} - \frac{\omega}{3}\,\frac{Ma_\Gamma}{3\mu+2}\,\frac{Bo}{Ca}\right)\hat{k}\right] + Pe_s^2\left[\frac{2}{3(3\mu+2)}\left(Ma_\Gamma\, I_{10}^{(2)} + \frac{2\omega\, Ma_\Gamma^2}{9(3\mu+2)^3}\,\frac{Bo}{Ca}\right)\hat{k}\right. \\ &\left. + \frac{2}{3(3\mu+2)}\left(Ma_\Gamma\, I_{11}^{(2)} - \frac{\omega b(5\mu+3)\, Ma_\Gamma}{45(3\mu+2)^2(\mu+1)R_0^2}\,\frac{Bo}{Ca}\right)\hat{i}\right] + O(Pe_s^3).\end{aligned} \tag{B2}$$

Since a centred monopole does not affect the migration velocity, (B2) is the same as the migration velocity obtained by Das *et al.* (2018).

For an off-centred monopole, the surfactant concentration is

$$\begin{aligned}\Gamma = 1 + Pe_s &\left[\left(I_{10}^{(1)} - \frac{3\kappa Sd\, Ma_T}{(\kappa+2)(3\mu+2)}\right)\cos\theta + I_{21}^{(1)}\cos\phi\, P_2^1(\cos\theta) + I_{30}^{(1)}\, P_3^0(\cos\theta)\right] \\ &+ Pe_s^2\left[\left(I_{10}^{(2)} + \frac{3\kappa Sd\, Ma_T\, Ma_\Gamma}{(\kappa+2)(3\mu+2)^2}\right)\cos\theta + I_{21}^{(2)}\cos\phi\, P_2^1(\cos\theta) + I_{30}^{(2)}\, P_3^0(\cos\theta)\right. \\ &+ \left(I_{11}^{(2)} - \frac{21\kappa Sdb(5\mu+3)\, Ma_T}{70(\kappa+2)(1+\mu)(3\mu+2)R_0^2}\right)\cos\phi\, P_1^1(\cos\theta) \\ &+ \left(I_{20}^{(2)} - \frac{\pi\kappa Sd\, Ma_T}{7(\kappa+2)(3\mu+2)}\right)P_2^0(\cos\theta) + I_{22}^{(2)}\cos(2\phi)\, P_2^2(\cos\theta) \\ &\left.+ \left(I_{31}^{(2)} + \frac{432\kappa Sdb\, Ma_T}{1080R_0^2(\kappa+2)(3\mu+2)(\mu+1)}\right)\cos\phi\, P_3^1(\cos\theta)\right] + O(Pe_s^3), \end{aligned} \tag{B3}$$

and the migration velocity follows:

$$\begin{aligned} U = &\left[1 - \left(\frac{b}{R_0}\right)^2 - \frac{2\mu}{(3\mu+2)R_0^2} + \frac{2(G+\kappa Sd)\, Ma_T}{(\kappa+2)(3\mu+2)} + \frac{2\omega}{3}\left(\frac{1+\mu}{3\mu+2}\right)\frac{Bo}{Ca}\right]\hat{k} \\ &+ Pe_s\left[\frac{2}{3(3\mu+2)}\, Ma_\Gamma\left(I_{10}^{(1)} - \frac{3\kappa Sd\, Ma_T}{(\kappa+2)(3\mu+2)} - \frac{\omega}{3}\,\frac{Ma_\Gamma}{3\mu+2}\,\frac{Bo}{Ca}\right)\right]\hat{k} \\ &+ Pe_s^2\left[\frac{2}{3(3\mu+2)}\, Ma_\Gamma\left(I_{20}^{(2)} - \frac{\pi\kappa Sd\, Ma_T}{7(\kappa+2)(3\mu+2)} + \frac{2\omega\, Ma_\Gamma^2}{9(3\mu+2)^3}\,\frac{Bo}{Ca}\right)\hat{k}\right. \\ &\left.+ \frac{2}{3(3\mu+2)}\, Ma_\Gamma\left(I_{11}^{(2)} - \frac{21\kappa Sdb(5\mu+3)\, Ma_T}{70(\kappa+2)(1+\mu)(3\mu+2)R_0^2} - \frac{\omega b(5\mu+3)\, Ma_\Gamma}{45(3\mu+2)^2(\mu+1)R_0^2}\,\frac{Bo}{Ca}\right)\hat{i}\right] \\ &+ O(Pe_s^3). \end{aligned} \tag{B4}$$

For a dipole, the surfactant concentration is

$$\begin{aligned}\Gamma = 1 + Pe_s &\left[\left(I_{10}^{(1)} - \frac{3\kappa S\cos\theta\, Ma_T}{(\kappa+2)(3\mu+2)}\right)\cos\theta + \left(-\frac{3\kappa S\sin\theta\, Ma_T}{(3\mu+2)(\kappa+2)}\right)\cos\phi\, P_1^1(\cos\theta)\right. \\ &\left.+ I_{21}^{(1)}\cos\phi\, P_2^1(\cos\theta) + I_{30}^{(1)}\, P_3^0(\cos\theta)\right] + Pe_s^2\left[\left(I_{10}^{(2)} + \frac{3\kappa S\cos\theta\, Ma_T\, Ma_\Gamma}{(\kappa+2)(3\mu+2)^2}\right)\cos\theta\right. \\ &+ I_{21}^{(2)}\cos\phi\, P_2^1(\cos\theta) + I_{30}^{(2)}\, P_3^0(\cos\theta) + \left(I_{11}^{(2)} - \frac{21\kappa S\cos\theta\, b(5\mu+3)\, Ma_T}{70(\kappa+2)(1+\mu)(3\mu+2)R_0^2}\right)\cos\phi \\ &\times P_1^1(\cos\theta) + \left(I_{20}^{(2)} - \frac{\pi\kappa S\cos\theta\, Ma_T}{7(\kappa+2)(3\mu+2)}\right)P_2^0(\cos\theta) + I_{22}^{(2)}\cos(2\phi)\, P_2^2(\cos\theta) \\ &\left.+ \left(I_{31}^{(2)} + \frac{432\kappa S\cos\theta\, b\, Ma_T}{1080R_0^2(\kappa+2)(3\mu+2)(\mu+1)}\right)\cos\phi\, P_3^1(\cos\theta)\right] + O(Pe_s^3), \end{aligned} \tag{B5}$$

and the migration velocity is

$$U = \left[\left(1-\left(\frac{b}{R_0}\right)^2 - \frac{2\mu}{(3\mu+2)R_0^2} + \frac{2(G+\kappa S\cos\theta)\,Ma_T}{(\kappa+2)(3\mu+2)} + \frac{2\omega}{3}\left(\frac{1+\mu}{3\mu+2}\right)\frac{Bo}{Ca}\right)\hat{k}\right.$$
$$\left. + \frac{2\kappa S\sin\theta\,Ma_T}{(\kappa+2)(3\mu+2)}\,\hat{i}\right] + Pe_s\left[\frac{2}{3(3\mu+2)}\,Ma_\Gamma\left(I_{10}^{(1)} - \frac{3\kappa S\cos\theta\,Ma_T}{(\kappa+2)(3\mu+2)} - \frac{\omega}{3}\,\frac{Ma_\Gamma}{3\mu+2}\right.\right.$$
$$\left.\left.\times\,\frac{Bo}{Ca}\right)\hat{k} - \frac{6\kappa S\sin\theta\,Ma_T\,Ma_\Gamma}{3(3\mu+2)^2(\kappa+2)}\,\hat{i}\right] + Pe_s^2\left[\frac{2}{3(3\mu+2)}\,Ma_\Gamma\left(I_{20}^{(2)} - \frac{\pi\kappa S\cos\theta\,Ma_T}{7(\kappa+2)(3\mu+2)}\right.\right.$$
$$\left. + \frac{2\omega\,Ma_T^2}{9(3\mu+2)^3}\,\frac{Bo}{Ca}\right)\hat{k} + \frac{2}{3(3\mu+2)}\,Ma_\Gamma\left(I_{11}^{(2)} - \frac{21\kappa S\cos\theta\,b(5\mu+3)\,Ma_T}{70(\kappa+2)(1+\mu)(3\mu+2)R_0^2}\right.$$
$$\left.\left. - \frac{\omega b(5\mu+3)\,Ma_\Gamma}{45(3\mu+2)^2(\mu+1)R_0^2}\,\frac{Bo}{Ca}\right)\hat{i}\right] + O(Pe_s^3). \tag{B6}$$

Here,

$$I_{10}^{(1)} = \frac{-3R_0^2 G\,Ma_T - 2(\kappa+2)}{(\kappa+2)(3\mu+2)R_0^2} - \frac{\omega}{3(3\mu+2)}\,\frac{Bo}{Ca}, \tag{B7}$$

$$I_{21}^{(1)} = -\frac{b}{3R_0^2(1+\mu)}, \tag{B8}$$

$$I_{30}^{(1)} = \frac{1}{6R_0^2(1+\mu)}, \tag{B9}$$

$$I_{10}^{(2)} = \frac{\omega}{3}\,\frac{Ma_\Gamma}{(3\mu+2)^2}\,\frac{Bo}{Ca} + \frac{[3R_0^2 G\,Ma_T + 2(\kappa+2)]Ma_\Gamma}{(3\mu+2)^2(\kappa+2)R_0^2}, \tag{B10}$$

$$I_{21}^{(2)} = -\frac{b\,Ma_\Gamma}{15R_0^2(1+\mu)^2}, \tag{B11}$$

$$I_{30}^{(2)} = -\frac{Ma_\Gamma}{42R_0^2(1+\mu)^2}, \tag{B12}$$

$$I_{11}^{(2)} = -V - \frac{b\,[21R_0^2(1+\mu)(5\mu+3)G\,Ma_T + (\kappa+2)(70\mu^2+109\mu+40)]}{70(\kappa+2)(1+\mu)^2(3\mu+2)R_0^4}, \tag{B13}$$

$$I_{20}^{(2)} = \frac{\omega^2}{27(3\mu+2)^2}\left(\frac{Bo}{Ca}\right)^2 + \frac{\pi}{21}[14XI_{10}^{(1)} - 6XI_{30}^{(1)} + 9(I_{21}^{(1)})^2 + 24I_{30}^{(1)}I_{10}^{(1)}$$
$$+ 4(I_{30}^{(1)})^2 - 21WI_{21}^{(1)}], \tag{B14}$$

$$I_{22}^{(2)} = -\frac{1}{252}\,\frac{(7\mu+4)b^2}{(1+\mu)^2R_0^4}, \tag{B15}$$

$$I_{31}^{(2)} = \frac{2\omega}{45}\,\frac{b}{R_0^2(3\mu^2+5\mu+2)}\,\frac{Bo}{Ca}$$
$$+\frac{b}{R_0^4}\left[\frac{432(1+\mu)R_0^2 G\,Ma_T + (45\mu^2+351\mu+310)(\kappa+2)}{1080(3\mu+2)(\mu+1)^2(\kappa+2)}\right], \tag{B16}$$

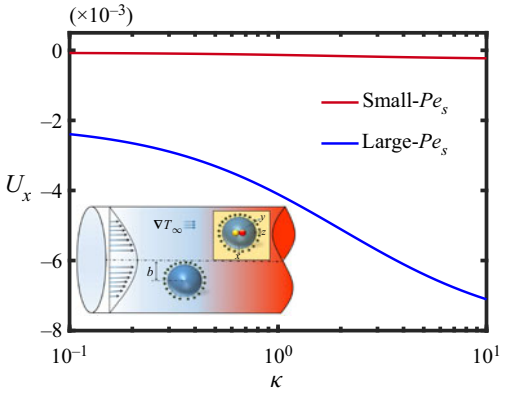

Figure 14. For both small- and large-Pe_s droplets, cross-stream migration velocity versus the thermal conductivity ratio κ is shown for the case of a streamwise oriented dipole. Other parameters are $S = 2$, $G = 1$, $Ma_\Gamma = 10$, $Ma_T = 1$, $b = 1$, $R_0 = 5$ and $Bo = 0$.

and

$$X = -\frac{3R_0^2 G\, Ma_T + 2(\kappa+2)}{(\kappa+2)(3\mu+2)R_0^2}, \quad W = \frac{b}{R_0^2}, \quad V = \frac{\omega b}{30R_0^2}\,\frac{5\mu+3}{3\mu^2+5\mu+2}\,\frac{Bo}{Ca}. \quad \text{(B17}a\text{–}c\text{)}$$

Appendix C. Comparative analysis of U_x with κ: small-Pe_s versus large-Pe_s limits

In figure 14, we have shown the variation of cross-stream migration velocity U_x with thermal conductivity ratio κ for both small- and large-Pe_s limits when the droplet is subjected to a streamwise oriented dipole. In the presence of an ambient thermal field along the Poiseuille flow ($G = 1$), U_x is negligibly small for small Pe_s, so the droplet is dominated by the streamwise migration. However, for large Pe_s, U_x varies significantly, so $|U_x|$ increases rapidly with increasing thermal conductivity ratio κ. In the latter case, due to the mass transfer boundary layer around the droplet, the impact of κ is significant, enhancing the temperature gradient between the droplet and the surrounding medium. Consequently, the stronger thermal gradient increases the Marangoni stress, which enhances the cross-stream migration velocity. Similar behaviour is observed for other thermal singularities also.

Appendix D. Small Pe_s analysis for a buoyant droplet ($Bo/Ca \neq 0$)

From (B2), (B4) and (B6), we note that though the buoyancy acts in the direction of Poiseuille flow (i.e. along z axis), it also affects the cross-stream migration velocity of the droplet, which is further enhanced due to the thermal singularities. We analyse the effect of buoyancy for the following cases: (i) $\omega = 1$, $G = 1$, which signifies that the buoyancy and the ambient thermal field act in the flow direction; (ii) $\omega = 1$, $G = -1$, which signifies that the buoyancy acts along the flow, but the temperature field direction is reversed; (iii) $\omega = -1$, $G = 1$, which means that the buoyancy force acts opposite to the flow, and the ambient temperature field is along the flow; and (iv) $\omega = -1$, $G = -1$, which indicates that the buoyancy and thermal field act opposite to the flow.

Figure 15(a) shows the variation of the cross-stream migration velocity U_x with the viscosity ratio μ when $Bo/Ca \neq 0$. The magnitude of the cross-stream migration velocity

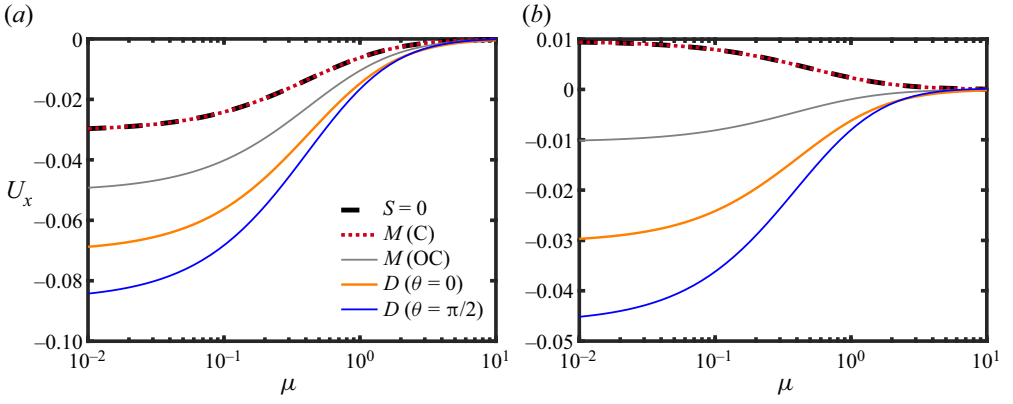

Figure 15. Droplet cross-stream migration velocity U_x versus viscosity ratio μ for $S = 0$ (dashed line), centred monopole (dotted line), off-centred monopole (grey), dipole oriented streamwise (orange) and dipole oriented transversely (blue), for (*a*) $G = 1$, $\omega = 1$, and (*b*) $G = -1$, $\omega = 1$. Other parameters are $S = 2$, $Ma_T = 1$, $Ma_\Gamma = 10$, $Pe_s = 0.1$, $\kappa = 1$, $b = 1$, $R_0 = 5$ and $Bo/Ca = 1$.

($|U_x|$) is observed to increase significantly compared to the case when $Bo/Ca = 0$ (as shown in figure 12*b*). This enhancement is due to the buoyancy force acting in the same direction as the applied temperature gradient and ambient flow. As a result, the Marangoni stress is amplified, causing the droplet to migrate faster towards the flow centreline. Now, when $G = -1$ and $\omega = 1$, from figure 15(*b*), we can observe that in the absence of a thermal singularity or in the case of a centred monopole (which has no impact on the migration velocity), the droplet moves away from the flow centreline. However, in the presence of an off-centred monopole or a dipole, the combined effect exerted on the droplet becomes stronger, resulting in its movement towards the centreline. Similar effects can also be observed in cases (iii) and (iv).

References

Ahn, K., Kerbage, C., Hunt, T.P., Westervelt, R.M., Link, D.R. & Weitz, D.A. 2006 Dielectrophoretic manipulation of drops for high-speed microfluidic sorting devices. *Appl. Phys. Lett.* **88** (2), 024104.

Anna, S.L. 2016 Droplets and bubbles in microfluidic devices. *Annu. Rev. Fluid Mech.* **48**, 285–309.

Balasubramaniam, R. & Chai, A.T. 1987 Thermocapillary migration of droplets: an exact solution for small Marangoni numbers. *J. Colloid Interface Sci.* **119** (2), 531–538.

Bandopadhyay, A., Mandal, S., Kishore, N.K. & Chakraborty, S. 2016 Uniform electric-field-induced lateral migration of a sedimenting drop. *J. Fluid Mech.* **792**, 553–589.

Baroud, C.N., Gallaire, F. & Dangla, R. 2010 Dynamics of microfluidic droplets. *Lab on a Chip* **10** (16), 2032–2045.

Baumgartner, D., Brenn, G. & Planchette, C. 2020 Effects of viscosity on liquid structures produced by in-air microfluidics. *Phys. Rev. Fluids* **5** (10), 103602.

Bratukhin, Y.K. 1975 Thermocapillary drift of a droplet of viscous liquid. *Fluid Dyn.* **10** (5), 833–837.

Choudhuri, D. & Raja Sekhar, G.P. 2013 Thermocapillary drift on a spherical drop in a viscous fluid. *Phys. Fluids* **25** (4), 043104.

Dandekar, R. & Ardekani, A.M. 2020 Effect of interfacial viscosities on droplet migration at low surfactant concentrations. *J. Fluid Mech.* **902**, A2.

Das, S., Mandal, S. & Chakraborty, S. 2018 Effect of temperature gradient on the cross-stream migration of a surfactant-laden droplet in Poiseuille flow. *J. Fluid Mech.* **835**, 170–216.

Grauer, J., Schmidt, F., Pineda, J., Midtvedt, B., Löwen, H., Volpe, G. & Liebchen, B. 2021 Active droploids. *Nat. Commun.* **12** (1), 6005.

Hanna, J.A. & Vlahovska, P.M. 2010 Surfactant-induced migration of a spherical drop in Stokes flow. *Phys. Fluids* **22** (1), 013102.

HAPPEL, J. & BRENNER, H. 1981 *Low Reynolds Number Hydrodynamics*. Springer.
HETSRONI, G. & HABER, S. 1970 The flow in and around a droplet or bubble submerged in an unbound arbitrary velocity field. *Rheol. Acta* **9** (4), 488–496.
HOMSY, G.M. & MEIBURG, E. 1984 The effect of surface contamination on thermocapillary flow in a two-dimensional slot. *J. Fluid Mech.* **139**, 443–459.
HUEBNER, A., SHARMA, S., SRISA-ART, M., HOLLFELDER, F., EDEL, J.B. & DEMELLO, A.J. 2008 Microdroplets: a sea of applications? *Lab on a Chip* **8** (8), 1244–1254.
KARABELAS, A.J. 1977 Vertical distribution of dilute suspensions in turbulent pipe flow. *AIChE J.* **23** (4), 426–434.
KAUSHAL, D.R. & TOMITA, Y. 2002 Solids concentration profiles and pressure drop in pipeline flow of multisized particulate slurries. *Intl J. Multiphase Flow* **28** (10), 1697–1717.
KIM, H.S. & SUBRAMANIAN, R.S. 1989 Thermocapillary migration of a droplet with insoluble surfactant: I. Surfactant cap. *J. Colloid Interface Sci.* **127** (2), 417–428.
LAMB, H. 1924 *Hydrodynamics*. Cambridge University Press.
LEAL, L.G. 2007 *Advanced Transport Phenomena: Fluid Mechanics and Convective Transport Processes*. Cambridge University Press.
LINK, D.R., GRASLAND-MONGRAIN, E., DURI, A., SARRAZIN, F., CHENG, Z., CRISTOBAL, G., MARQUEZ, M. & WEITZ, D.A. 2006 Electric control of droplets in microfluidic devices. *Angew. Chem. Intl Ed.* **45** (16), 2556–2560.
MANIKANTAN, H. & SQUIRES, T.M. 2020 Surfactant dynamics: hidden variables controlling fluid flows. *J. Fluid Mech.* **892**, P1.
MARCHETTI, M.C. 2012 Spontaneous flows and self-propelled drops. *Nature* **491** (7424), 340–341.
NALLANI, M. & SUBRAMANIAN, R.S. 1993 Migration of methanol drops in a vertical temperature gradient in a silicone oil. *J. Colloid Interface Sci.* **157** (1), 24–31.
PADMAVATHI, B.S., RAJA SEKHAR, G.P. & AMARANATH, T. 1998 A note on complete general solutions of Stokes equations. *Q. J. Mech. Appl. Maths* **51** (3), 383–388.
PAK, O.S., FENG, J. & STONE, H.A. 2014 Viscous Marangoni migration of a drop in a Poiseuille flow at low surface Péclet numbers. *J. Fluid Mech.* **753**, 535–552.
PALANIAPPAN, D., NIGAM, S.D., AMARANATH, T. & USHA, R. 1992 Lamb's solution of Stokes's equations: a sphere theorem. *Q. J. Mech. Appl. Maths* **45** (1), 47–56.
PANIGRAHI, D.P., SANTRA, S., BANUPRASAD, T.N., DAS, S. & CHAKRABORTY, S. 2021 Interfacial viscosity-induced suppression of lateral migration of a surfactant laden droplet in a nonisothermal Poiseuille flow. *Phys. Rev. Fluids* **6** (5), 053603.
RAJA SEKHAR, G.P., RAO, K.T., PADMAVATHI, B.S. & AMARANATH, T. 1995 Two dimensional Stokes flows with slip–stick boundary conditions. *Mech. Res. Commun.* **22** (5), 491–501.
RAJABI, M., BAZA, H., TURIV, T. & LAVRENTOVICH, O.D. 2021 Directional self-locomotion of active droplets enabled by nematic environment. *Nat. Phys.* **17** (2), 260–266.
RAMOS, G., CORDERO, M.L. & SOTO, R. 2020 Bacteria driving droplets. *Soft Matt.* **16** (5), 1359–1365.
REDNIKOV, A.E. & RYAZANTSEV, Y.S. 1989 On the thermocapillary motion of a drop with homogeneous internal heat evolution. *J. Appl. Maths Mech.* **53** (2), 212–216.
ROTHBAUM, H.P. & STONE, H.M. 1961 Heat output of *Escherichia coli*. *J. Bacteriol.* **81** (2), 172–177.
SADHAL, S.S. & JOHNSON, R.E. 1983 Stokes flow past bubbles and drops partially coated with thin films. Part 1. Stagnant cap of surfactant film – exact solution. *J. Fluid Mech.* **126**, 237–250.
SADHAL, S.S. & JOHNSON, R.E. 1986 On the deformation of drops and bubbles with varying interfacial tension. *Chem. Engng Commun.* **46** (1–3), 97–109.
SCHWALBE, J.T., PHELAN, J., FREDERICK, R., VLAHOVSKA, P.M. & HUDSON, S.D. 2011 Interfacial effects on droplet dynamics in Poiseuille flow. *Soft Matt.* **7** (17), 7797–7804.
SEEMANN, R., BRINKMANN, M., PFOHL, T. & HERMINGHAUS, S. 2011 Droplet based microfluidics. *Rep. Prog. Phys.* **75** (1), 016601.
SHANKAR, S., RAJU, V. & MAHADEVAN, L. 2022 Optimal transport and control of active drops. *Proc. Natl Acad. Sci.* **119** (35), e2121985119.
SHARANYA, V. & RAJA SEKHAR, G.P. 2015 Thermocapillary migration of a spherical drop in an arbitrary transient Stokes flow. *Phys. Fluids* **27** (6), 063104.
SHARANYA, V., RAJA SEKHAR, G.P. & ROHDE, C. 2019 Surfactant-induced migration of a spherical droplet in non-isothermal Stokes flow. *Phys. Fluids* **31** (1), 012110.
SNEDDON, I.N. 2006 *Elements of Partial Differential Equations*. Dover.
STAN, C.A., GUGLIELMINI, L., ELLERBEE, A.K., CAVIEZEL, D., STONE, H.A. & WHITESIDES, G.M. 2011 Sheathless hydrodynamic positioning of buoyant drops and bubbles inside microchannels. *Phys. Rev.* E **84** (3), 036302.

STONE, H.A. 1990 A simple derivation of the time-dependent convective–diffusion equation for surfactant transport along a deforming interface. *Phys. Fluids* A **2** (1), 111–112.

STONE, H.A. & LEAL, L.G. 1990 The effects of surfactants on drop deformation and breakup. *J. Fluid Mech.* **220**, 161–186.

STONE, H.A. & MASOUD, H. 2015 Mobility of membrane-trapped particles. *J. Fluid Mech.* **781**, 494–505.

STONE, H.A., STROOCK, A.D. & AJDARI, A. 2004 Engineering flows in small devices: microfluidics toward a lab-on-a-chip. *Annu. Rev. Fluid Mech.* **36**, 381–411.

SUBRAMANIAN, R.S. 1983 Thermocapillary migration of bubbles and droplets. *Adv. Space Res.* **3** (5), 145–153.

SUBRAMANIAN, R.S. & BALASUBRAMANIAM, R. 2001 *Motion of Bubbles and Drops in Reduced Gravity*. Cambridge University Press.

TEH, S.Y., LIN, R., HUNG, L.H. & LEE, A.P. 2008 Droplet microfluidics. *Lab on a Chip* **8** (2), 198–220.

THOMPSON, R.L., DEWITT, K.J. & LABUS, T.L. 1980 Marangoni bubble motion phenomenon in zero gravity. *Chem. Engng Commun.* **5** (5–6), 299–314.

YOUNG, N.O., GOLDSTEIN, J.S. & BLOCK, M. 1959 The motion of bubbles in a vertical temperature gradient. *J. Fluid Mech.* **6** (3), 350–356.

ZHU, Y. & FANG, Q. 2013 Analytical detection techniques for droplet microfluidics – a review. *Anal. Chim. Acta* **787**, 24–35.